Synaptic spine head morphodynamics from graph grammar rules for actin dynamics

Matthew Hur[1], Thomas M. Bartol[2], Padmini Rangamani[3], Terrence J. Sejnowski[2,4], Eric Mjolsness[5,*]

[1]Program in Mathematical, Computational, and Systems Biology, University of California, Irvine, Irvine, 92697, CA, USA.
[2]Computational Neurobiology Laboratory, Salk Institute for Biological Studies, La Jolla, 92037, CA, USA.
[3]Departments of Pharmacology and Mechanical and Aerospace Engineering, University of California, San Diego, La Jolla, 92093, CA, USA.
[4]Department of Neurobiology, University of California, San Diego, La Jolla, 92093, CA, USA.
[5]Departments of Computer Science and Mathematics, University of California, Irvine, Irvine, 92697, CA, USA.

*Corresponding author(s). E-mail(s): emj@uci.edu;
Contributing authors: hurm1@uci.edu; bartol@salk.edu; padmini.rangamani@eng.ucsd.edu; terry@salk.edu;

Abstract

There is a morphodynamic component to synaptic learning by which changes in dendritic (postsynaptic) spine head size are associated with the strengthening or weakening of the synaptic connection between two neurons. The membrane shape and size dynamics is sculpted by the growth dynamics of the enclosed actin cytoskeleton. We use Dynamical Graph Grammars (DGGs) governing dynamic labelled graphs embedded in two dimensions to model networks of actin filaments and the enclosing membrane in spine head morphology. We demonstrate the flexibility and extensibility of the framework by encoding detailed biophysical as well as biochemical models, obeying constraints of invariance and conservation, in DGG rule sets. From graph-local energy functions for cytoskeleton actin interacting and membrane, we specialize dissipative stochastic dynamics to an exhaustive collection of graph-local neighborhood types for the rule left

hand sides. Extensively simulating the resulting model delineates effects of four actin-binding proteins, and their epistatic relationships, on morphology.

Keywords: spine head, actin, simulation, biophysics, epistasis, graph grammar, membrane

1 Introduction

Actin cytoskeletal dynamics leads to changes in the shape of cells through action on the membranes of signal-receiving neuronal compartments called dendritic spine heads ([1]). Synaptic spine heads influence learning because their size influences the strength of the synaptic connection between two neurons ([2]). Repeated firing across the same synapse can lead to a long-lasting connection in the form of memory, as in Hebbian learning ([3]). Models of the synaptic spine head hold potential to model behaviors such as addiction and have been posited to be explanatory for the engram hypothesis in how memory is stored in the brain ([4–6]). Actin's importance in synaptic biophysical kinetics can lead to understanding of biological memory and learning, as well as to potential therapeutics ([7]).

Actin filament biophysics can be modeled from principles that incorporate mechanical memory of signaling from neuron to neuron. A system dependent on a global, anharmonic energy potential can lead to many energy minima consistently arising. The wells of the energy potentials are positioned nearby a filament's axis. Spatial transitions between them create a memory system that involves a dynamic system of moving wells of energy. The CaMKIIβ molecule is a bundling protein that strengthens individual chains of actins by cross-linking them ([8]). Its binding to the filament form of actin (F-actin) thus leads to stronger filaments ([9]). CaMKIIβ's binding along actin filaments allows the intermolecular potentials to exert a force on the connected nodes of the bundling link.

Prior actin models have been implemented in niche simulation packages such as Cytosim ([10, 11]), but they make assumptions about biophysical filament systems that can be fully accounted for using a declarative and highly expressive simulation package based on DGGs ([12]). Moving boundaries have been approached as part of hybrid models, e.g. partial differential equations ([13]) with finite element methods ([14]). Yet, these approaches may lack the ability to impose complex biophysical constraints through simple local rules, or they lack fine-granularity in either the internal cytoskeleton or the forces onto the membrane mesh. What is needed is a graph-based approach that can downscale the granularity of the internal cytoskeleton representation and that enables easy expression of biophysical complexities such as membrane mesh dynamics including for example the Newtonian reaction forces between the cytoskeleton and membrane.

In order to simulate actin taking into account connectivity of an actin network, we build a model as a Dynamical Graph Grammar (DGG) ([12]) implemented in a computer algebra system in which expressive rules are written for pattern matching in the underlying package. DGGs are theoretically grounded ([15]) and originate as

a graph-based notational extension of Stochastic Parameterized Grammars (SPGs) which, highly expressive by nature, is applied to node-labeled multisets instead of graphs, and incorporates probability distributions over rule firings and their outcomes ([16]). DGGs also incorporate differential equation dynamics.

As we apply biophysical rules that move objects parameterized with spatial positions, we explain the relevance of simulating in an expressive and declarative theory-based modeling language that is grounded in particle physics theory ([15]). The creation and annihilation paradigm, which correspond to graph operations, implemented computationally, can apply to dynamical graphs. This is similar to how the operators of the paradigm apply to the statistical mechanics of particles such as the general set of fermion particles. Relaxing constraints – as the DGG derives from application to node-labeled multisets and from creation/annihilation particle operators of studied fermions – allows a wide range of criteria for DGG use-cases. Important to this study, spatial simulations and high-performance computing (HPC) are included in those criteria ([15]).

Here, hundreds of mathematical rules expressed in Plenum, a Mathematica package that implements DGGs ([17]), model the behavior of the actin network remodeling, biophysical kinetics, and interaction with membrane, while the membrane has its own rules for curvature updates. We show that we are able to simulate a dynamically changing cellular protrusion within reasonable time scales using the highly expressive DGG package Plenum in the Mathematica computer algebra system ([17]).

Our work complements prior modeling of synaptic spine heads based on differential equations that model the actin cytoskeleton. Previously, there has been work on modeling actin cytoskeleton forces exerted onto synaptic spine membranes using differential equations ([13, 18, 19]). In our work, we implement the Brownian ratchet (BR) hypothesis which posits that fluctuations in both the lipid bilayer and ends of actin filaments lead to large enough distances between them for actin to polymerize ([20]). This polymerization then provides force onto the membrane. Previous models, with a membrane, coarse-grain membrane-filament interaction as a spring attachment without BR ([21]) and others, along with the coarse inter-module interaction, use a partial membrane section in the simulations for endocytosis ([22, 23]). Thus, the cell's morphology is treated as a plane with mainly barbed end mechanics in comparison to our fully enclosed circular compartment of the dendritic spine head. To accurately capture biophysical memory effects, we implement anharmonic potentials ([24]) that can have multiple, spatially dependent energy wells and are designed, through DGG rules, to follow biophysical constraints and laws. The anharmonic potential thermal movement, e.g. generated by friction within the highly viscous spine head medium, exhibits memory friction ([24, 25]) similar to in this paper implicitly. Implementation within the well-founded DGG framework may also, in future, allow theoretical advances ([12, 26]) such as model reduction to be applied to the dendritic spine head rule system.

In this paper, we show that we can build a model for simulation of physical interaction between the actin cytoskeleton and the membrane using DGGs, and within a plausible model we can functionally characterize actin binding proteins (ABPs) that bind to and modulate individual actin monomers, affecting membrane shape. This

framework can be used to grow an entire spine head from a membrane-enclosed area, though all in two dimensions for simplicity and computational tractability.

While in the past DGGs have been used in non-biophysical simulation of microtubules ([27]), using it with the biophysical kinetics of fibers and membranes in an agent-based simulation as presented in this paper is novel. (By "biophysical kinetics", hereinafter just "biophysics", we refer to the dynamics of spatial positions of particles and elements of extended objects such as fibers and membranes, all due to position-dependent forces.) We consider the propulsive force of a cytoskeleton onto a membrane polygon and the respective Newtonian reaction force of the membrane onto the cytoskeleton polymers in determining the inter-module dynamics of the system. In simulating the spatial movement of the cytoskeleton, we hope to gain a better and more accurate understanding of how the actin cytoskeleton determines shape and size of a cellular protrusion.

2 Results

2.1 DGG simulations represent growth of synaptic spine heads

We implement a DGG model inside a simulator in Plenum that minimizes the biophysical energy of a dynamically changing network. The total energy function is shown in Eq. 1

$$\begin{aligned} E_{\text{tot}} = & \underbrace{\sum_{i,j\neq i}^{N} G_{ij} U_{\text{sep}}(x_i, x_j)}_{\text{Anisotropic Buckling}} + \underbrace{\sum_{i\neq j\neq k\neq i}^{N} G_{ij} G_{jk} U_{\text{ang}}(x_i, x_j, x_k, \theta_{\text{target}})}_{\text{Angular Bending Energy}} \\ & + \underbrace{2\kappa \sum_{a\neq b\neq c\neq a}^{M} g_{ab} g_{bc} H^2_{\Gamma(x_a, x_b, x_c)}}_{\text{Membrane Mean Helfrich Energy}} . \end{aligned} \tag{1}$$

In this formula, G denotes the adjacency matrix of an actin cytoskeleton network's graph representation, and g denotes that for an enclosing membrane mesh. The membrane term is mediated by a directed graph with adjacency matrix g_{bc} which consists of the counterclockwise cycle of edges around the 1D membrane embedded in 2D space.

Simulations run up to 60 seconds of biological time achieve compartment growth up to 20% in Fig. I. An area of 0.048 μm^2 roughly corresponds to the transverse cross-sectional area of a biological synaptic spine head ([28]). This indicates the possibility of simulating the effects of long-term potentiation (LTP) from repeated electrical signals that mediate Hebbian learning as in [13].

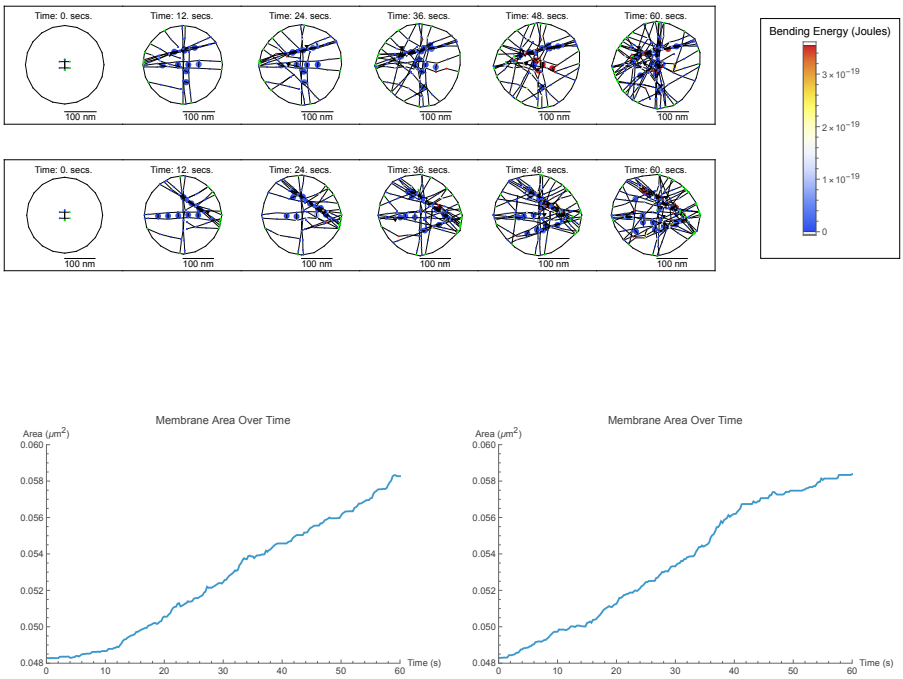

Fig. I:
Top: Snapshots of two stochastic simulations of the stubby synaptic spine head. Simulation snapshots evolve from the same initial condition from stochastic variability. Model includes Aip1. Color indicates the degree of angle bending energy (or green for a barbed end) for each object, circles represent coarse-grained actin objects ($N_{\mathrm{CG}} = 12$), triangles represent caps or colored triangles represent junction objects, and dodecagons represent CaMKIIβ bundling complexes.
Bottom: Membrane-enclosed area over time. Plots arranged from left-to-right correspond to simulations arranged top-to-bottom.

Dendritic spines belong to a few types based on their shapes (i.e. stubby, mushroom, thin, filopodia, branched) ([29]). In this paper, we investigate the spine head at an actin synthesis rate specific to the stubby type ([30]). Of the types, the stubby spine type is in a more expansive growth phase, able to readily develop into more mature spines. Mushroom spines are known as mature "memory spines" because they are considered the developed type, with markers of past growth stored in the internal actin cytoskeleton ([31]). We characterize the stubby spine type further through parameter sweeps, including spine type specific effects for the four ABPs (Arp2/3, CaMKIIβ, cofilin, Aip1), by varying their synthesis rates.

In all our simulations in this paper, synthesis rates are altered from their estimated basal values from [32] that are from differential equations in [13], by adding and subtracting additional rates estimated from the same ODEs. The set of estimated synthesis rates is pursuant to the glutamate uncaging model in the [32] study. As glutamate stimulates the synaptic spine in this model, it grows to a larger stable size for spine head size in a process known as long-term potentiation (LTP) ([33]). LTP is part of learning and memory ([34]).

Biologically, neurotransmitters reaching ligand-gated ion channels on the membrane of the postsynaptic terminal can elevate the concentration of proteins related to the actin cytoskeleton ([35]). Synthesis rates can increase or decrease from influx due to electrical stimuli, which trigger the release of neurotransmitters, responding to different neuronal firing rates.

We include four ABPs in our simulation model. Here, we list their individual, putative functions, which may interact with each other such as by competitive binding and will be explored in computer simulations. Arp2/3 creates other F-actin filament branches off of F-actin filaments, CaMKIIβ bundles separate F-actin filaments, and cofilin and Aip1 sever F-actin filaments in a joint mechanism.

In the parameter sweep shown in Fig. II for stubby spine heads, we see that as the synthesis rates of cofilin, Arp2/3, and CaMKIIβ concentration increase, they increase (Arp2/3 with $p = 0.0074$; CaMKIIβ with $p = 0.00030$; Aip1 with $p = 0.00048$; in Table I) and decrease (cofilin with $p = 0.033$; in Table I) spine head size. In all cases we consider a statistical test p-value of < 0.05 to be "significant".

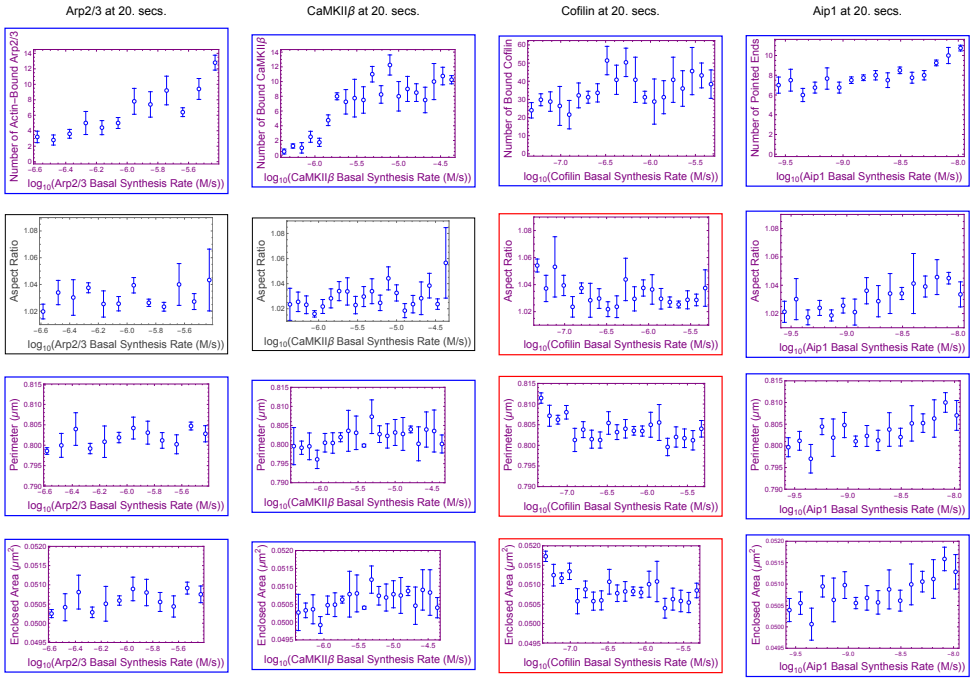

Fig. II: Dependence of membrane properties on synthesis rates of four actin-binding regulatory proteins demonstrated in parameter sweeps. The basal synthesis rate provided in Section 4 Table IV is the middle value for cofilin and CaMKIIβ horizontal-axes. Error bars show standard error of the mean (SEM) with Bessel's correction, for a number of stochastic simulations each. We calculate membrane aspect ratio, membrane perimeter, and membrane enclosed area for each simulation snapshot. The number of simulations is 5 for Arp2/3 and cofilin and 4 for CaMKIIβ and Aip1, corresponding to each mean value with error bar in the plots. Indigo graphs are significant under p-value threshold 0.05. For the frames surrounding significant individual plots, blue is a significant increasing trend, and red is a significant decreasing trend as determined by Table I. The range on log-scale for the parameter sweep consists of 10× smaller to at most 10× larger than the estimated, basal synthesis rates for CaMKIIβ and cofilin, with range truncated at the upper end for Arp2/3 and Aip1. Rows represent membrane properties across four ABPs and columns represent a cytoskeletal network property followed by three membrane properties for each ABP.

2.2 Epistasis and antagonism between Arp2/3 and CaMKIIβ

In our stubby spine head simulations, interaction occurs between CaMKIIβ and Arp2/3. Our implementation of mutually exclusive binding at actin nodes for CaMKIIβ and Arp2/3 is observed in biological experiment ([36]). Since we are measuring several somatic "phenotypes"–which are membrane aspect ratio, membrane

Stubby spine head at 20.0 seconds				
Membrane property / value type	Arp2/3 (n=5)	CaMKIIβ (n=4)	cofilin (n=5)	Aip1 (n=4)
Aspect ratio / Jonckheere-Terpstra p-value	0.26	0.077	**0.015**	**0.00030**
— / Pearson's correlation p-value	0.68	0.074	**0.015**	**0.00020**
— / Pearson's correlation r-value	-0.045	0.23	-0.20	0.41
Perimeter / —	**0.010**	**0.039**	**0.00050**	**0.00071**
— / —	0.062	0.074	**0.0013**	**0.00020**
— / —	0.20	0.20	-0.32	0.45
Enclosed area / —	**0.0074**	**0.033**	**0.00030**	**0.00048**
— / —	**0.044**	**0.050**	**0.00074**	**0.00018**
— / —	0.22	0.22	-0.33	0.45

Table I: Statistical values for monotonicity and correlation in parameter sweeps of stubby spine heads. Jonckheere-Terpstra p-values are calculated using "jonckheereTest" in the "PMCRPlus" package of the R programming language. Stubby statistical values match the format of the parameter sweep of Fig. II. Trend tests for monotonicity, p-values < 0.05 are bold under the Jonckheere 1-sided test, with sidedness determined by the sign of Pearson's r in a linear fit.

perimeter, and membrane enclosed area– that could be exposed to selection, a genetic analysis approach (genotype to phenotype, skipping the complex system and model in between) such as epistasis is appropriate. The approach to epistasis in this paper is to elevate or lower synthesis rate of an ABP, e.g. CaMKIIβ, by a factor η^q, $q \in \{1, 2, 4\}$, and concomitantly increase Arp2/3 by a factor of η.

In our computational model, we include the actin filament bundling protein CaMKIIβ. During a situation like LTP, CaMKIIβ is known to unbind from the actin cytoskeleton because of an influx of calcium ions into the synaptic spine head that bind the Calmodulin (CaM) protein and reduce binding affinity of CaMKIIβ for actin filaments ([37]). Fig. IX shows the decrease in concentration of CaMKIIβ during a biological model of LTP by glutamate uncaging as done in [32]. We model this change to CaMKIIβ by fitting an ODE provided in [13] to data in [32]. From the fit, we arrive at a value for CaMKIIβ synthesis change during a model of LTP that is negative (Fig. IX and $k_{\text{influx, CaMKII}\beta}$ in Table IV). The negative value augmentation to CaMKIIβ synthesis influences the binding rate of CaMKIIβ by having less free CaMKIIβ available during simulation. Based on this phenomenon for CaMKIIβ, our subsequent simulation experiments will be under assumption that Arp2/3 synthesis increases and CaMKIIβ synthesis decreases during the model of LTP.

To clearly observe a phenotype, we have activated changes to synthesis rates in our model pursuant to glutamate uncaging and to long-term potentiation (LTP) induction, including decreasing CaMKIIβ synthesis rate and increasing Arp2/3 synthesis rate by 10× that decrease to CaMKIIβ. This ratio is estimated from fitting ODEs designed in [13] to published data in [32]. Now, as we apply the method of epistatic analysis, presented in [38], we assume that there is an interaction between Arp2/3 and CaMKIIβ based on our implementation of mutually exclusive binding. In a double parameter sweep (Fig. III), only Arp2/3 and CaMKIIβ determine the change to spine head morphology. Cofilin and Aip1 are under control conditions for LTP in the parameter sweeps for Arp2/3 and CaMKIIβ in Fig. II and in those in Fig. III. We will provide evidence from observations, in Fig. III and Fig. IV parameter sweeps, that Arp2/3 masks the effect of spine head growth by CaMKIIβ observed in second column of Fig. II ($r = 0.22$ and $p = 0.033$; in Table I). By continuing to argue that this observation

of masking is one-way and directional, we will show that Arp2/3 stops the effect of CaMKIIβ synthesis on spine head morphology through an epistasis of Arp2/3 on CaMKIIβ, during growth similar to LTP.

Here, we will show that Arp2/3 masks CaMKIIβ to show a condition in masking that is necessary for epistasis, but not yet totally sufficient, using data for nullification summarized in Table II and presented in Fig. III. To be a sufficient explanation for epistasis, the interpretation should conclude both masking, shown in this paragraph, and uni-directionality. As shown in column one of Fig. III, which corresponds to $q = 1$, Arp2/3 and CaMKIIβ can nullify each other's effect on spine head area (r = -0.065 and p = 0.47; in Table II). This null relationship is roughly expected at q value of one by its implied setting of synthesis rates at a nullification 1:1 log-ratio (Arp2/3 increased in steps of η^1 and CaMKIIβ in steps of $1/\eta^1$) and by data showing that CaMKIIβ affects spine head size in an approximately 1:1 log-ratio to Arp2/3 (r = 0.22 for Arp2/3 and r = 0.22 for CaMKIIβ area; r = 0.20 for Arp2/3 and r = 0.20 for CaMKIIβ perimeter; with p-values < 0.05; in Table I). Arp2/3 nullifies CaMKIIβ not only at $q = 1$, but also at $q = 2$ and $q = 4$ (p = 0.38 for power of two; p = 0.33 for power of four; for area in Table II with η applied to CaMKIIβ). The masking effect is measured by our simulation parameter sweeps starting by assuming an additive nullifiction effect. The starting 1:1 log-ratio is implied by data summarized in Table I from sweeps of Arp2/3 and CaMKIIβ alone (Fig. II). As the log-ratio favors CaMKIIβ synthesis value in ratios 1:2 ($q = 2$) and 1:4 ($q = 4$), the correlation r-value between Arp2/3 and CaMKIIβ, stays near-zero (r = 0.032 for $q = 2$ and r = -0.077 for $q = 4$) as it does for $q = 1$ (r = -0.065). As no value for q tested by applying to CaMKIIβ penetrates the nullification phenotype between Arp2/3 and CaMKIIβ, we can interpret that Arp2/3 masks phenotypic spine head growth effort by CaMKIIβ existing in column two of Fig. II (r = 0.22, p = 0.033; in Table I). In stubby spine head simulations, we show that Arp2/3 can mask CaMKIIβ mediated effect on spine heads.

Next, we will show that Arp2/3 uni-directionally masks CaMKIIβ, implied by data showing that Arp2/3 can penetrate the nullification in spine head growth of the log-ratio 1:1 between Arp2/3 and CaMKIIβ. Arp2/3 synthesis changes spine head size regardless of the increase or decrease applied to CaMKIIβ synthesis, different from the masking effect we observed onto CaMKIIβ that is explained in the previous paragraph. We observe this evidence for one-way directionality in masking. The supporting data is the significant correlation between Arp2/3 or CaMKIIβ synthesis and their effects on spine head growth in Fig. IV for higher gradations of change to Arp2/3 synthesis than to CaMKIIβ. Past the previously observed nullification value of $q = 1$, Arp2/3 significantly increases spine head size at the higher gradation values of $q \in \{2, 4\}$ (r = 0.17 and p = 0.031 for η^2; r = 0.41 and p = 0.00069 for η^4; in Table II). The presence of an effect for synthesis multiplier η^q favoring gradation of Arp2/3 synthesis demonstrates that Arp2/3 successfully penetrates the phenotypic nullification for concomitant and opposite gradation of CaMKIIβ synthesis. The penetrance effect by Arp2/3 indicates that CaMKIIβ does not mask phenotypic effect in spine head size by Arp2/3 synthesis change. Only Arp2/3 masks CaMKIIβ and not CaMKIIβ for Arp2/3, which indicates Arp2/3 is epistatic to CaMKIIβ during stubby spine head growth phase, in a model implemented for similarity to LTP.

Earlier in section 2.2, we show that because of epistasis, we can mask a CaMKIIβ effect on spine head growth by an opposite effect by Arp2/3. CaMKIIβ synthesis change alone would otherwise effect spine head size, an observation supported by biological experiment in [39]. Some studies report that bound amount of CaMKIIβ correlates with spine head size ([40, 41]). This relationship is consistent with what we observe about CaMKIIβ in Fig. II column two.

An alternative hypothesis is that the difference in binding energies of Arp2/3 and CaMKIIβ, represented by their dissociation constants (K_D), accounts for the competition, where k_{off} for Arp2/3 is not the unbinding rate of unitary Arp2/3, but the debranching rate of daughter filaments. Here, $K_{D,\ \text{CaMKII}\beta} = \frac{k_{\text{off, CaMKII}\beta}}{k_{\text{on, CaMKII}\beta}} = \frac{0.23\ (1/\text{s})}{0.5\times10^6\ (1/(\text{M s}))} \approx .46\ \mu\text{M}$ and $K_{D,\ \text{Arp2/3}} = \frac{k_{\text{off, Arp2/3}}}{k_{\text{on, Arp2/3}}} = \frac{2\times10^{-3}\ (1/\text{s})}{3000\ (1/(\text{M s}))} \approx .67\ \mu\text{M}$. By these K_D values, Arp2/3 and CaMKIIβ have similar K_Ds, which rules out binding energy as an explanation for our observation of epistasis.

Below, we show mathematical reasoning for double parameter sweeps as evidence for epistasis in addition to antagonism. Let $\alpha = \log_{10}(\text{Arp2/3 synthesis rate})$ and $\gamma = \log_{10}(\text{CaMKII}\beta\text{ synthesis rate})$ be the change in system variables by taking the logarithms of Arp2/3 and CaMKIIβ synthesis rates. If

$$\frac{d\ \text{phenotype}}{d\alpha} \Big/ \frac{d\ \text{phenotype}}{d\gamma} \approx -q, \tag{2}$$

we can introduce a new variable μ, to be varied, such that in the case of antagonism

$$\frac{d\alpha}{d\mu} \Big/ \frac{d\gamma}{d\mu} = (1/2)/(q/2) = 1/q. \tag{3}$$

A reversal of the powers of η applied to α and γ leads to the same method for change of variables. We find that $q = -1$ by substituting 0.22 and 0.22 from Table I for the numerator and denominator in Eq. (2). $q = -1$ represents the nullification observed between Arp2/3 and CaMKIIβ. In Table II, we have that higher values of q show masking that indicates more than nullification at those higher values of $|q|$. CaMKIIβ is unable to raise an effect due to rising Arp2/3 at the same steps of applying η to Arp2/3 and $1/\eta^q$ to CaMKIIβ; hence, the masking in this case is epistasis.

The reverse situation, with a reverse 2D change of variables, is different. α dominates at all higher q so γ cannot be epistatic to it.

Here, μ is the variable that is varied in the η parameter sweeps, i.e. in Fig. III– V. If Equations (2) and (3) are satisfied, for a set of axes in which μ is varied, then

$$\frac{d\ \text{phenotype}}{d\alpha}\frac{d\alpha}{d\mu} + \frac{d\ \text{phenotype}}{d\gamma}\frac{d\gamma}{d\mu} = 0, \tag{4}$$

which demonstrates nullification of the γ species by the α species (Fig. III) under these conditions.

To show the existence of such a variable μ, consider the 2D linear change of variables $\mu = \alpha + \frac{1}{q}\gamma$ and $\nu = \alpha - \frac{1}{q}\gamma$. Inverting the change of variables, $\alpha = (\mu + \nu)/2$ and $\gamma = (q/2)(\mu - \nu)$.

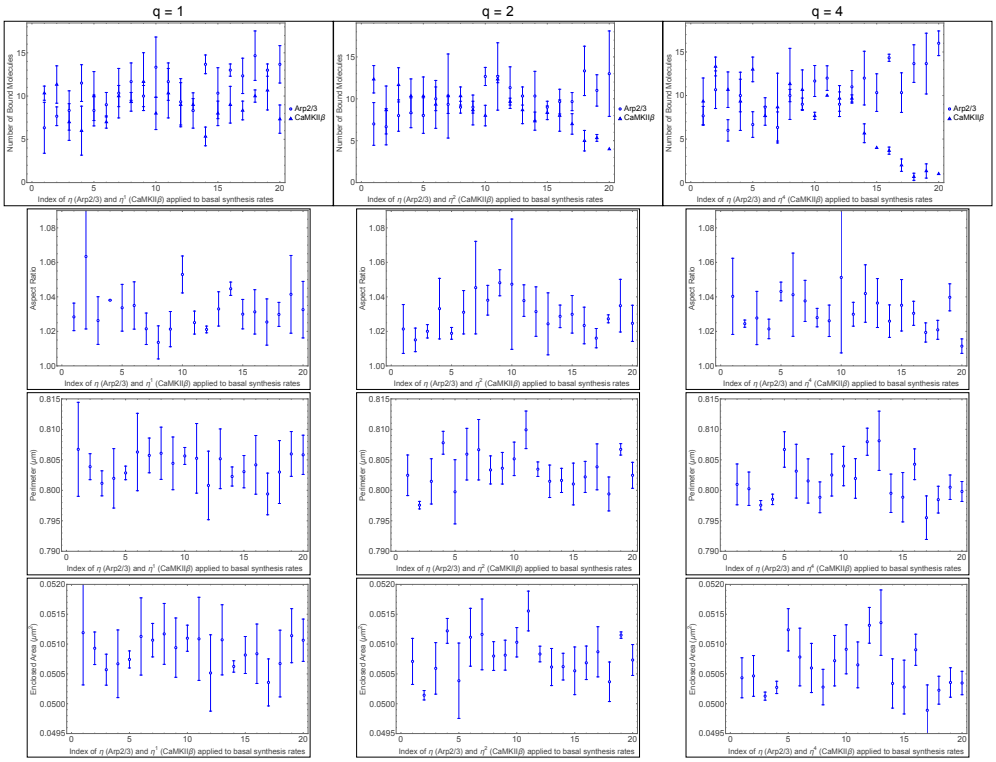

Fig. III: Epistatic masking of Arp2/3 on CaMKIIβ in the stubby spine head: Dependence of membrane properties on synthesis rates of CaMKIIβ and Arp2/3 demonstrated in parameter sweeps. η is directly applied to Arp2/3 synthesis, and η (first column), η^2 (middle column), and η^4 (last column) are applied to CaMKIIβ synthesis in reverse to test for epistatic nullification. CaMKIIβ synthesis is decreased by succesive applications of $1/\eta^q$ and Arp2/3 synthesis is increased by successive applciations of η. For a chosen multiplicative value of η, it is sequentially multiplied or divided to the original, basal synthesis rates, but at different powers of η for CaMKIIβ or Arp2/3, informed by the statistical values in Table I. The basal synthesis rates provided in Table IV are the middle values of the horizontal-axes. Error bars show standard error of the mean (SEM) with Bessel's correction for n = 3 simulations per data point.

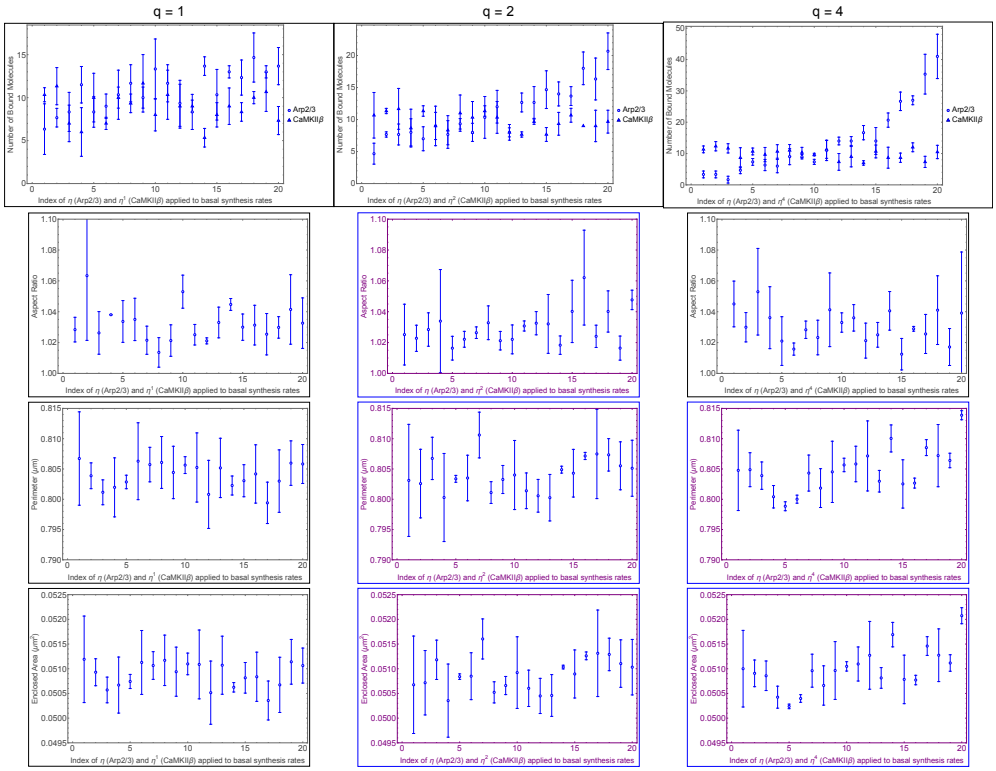

Fig. IV: Masking effect's uni-directionality of Arp2/3 on CaMKIIβ in the stubby spine head: Dependence of membrane properties on synthesis rates of CaMKIIβ and Arp2/3 demonstrated in parameter sweeps. CaMKIIβ synthesis is decreased by succesive applications of $1/\eta$ and Arp2/3 synthesis is increased by successive applciations of η^q. η is applied in reverse to CaMKIIβ synthesis, and η (first column), η^2 (middle column), and η^4 (last column) are directly applied to Arp2/3 synthesis to test for epistatic direction. For a chosen multiplicative value of η, it is sequentially multiplied or divided to the original, basal synthesis rates, but at different powers of η for CaMKIIβ or Arp2/3, informed by the statistical values in Table I. The basal synthesis rates provided in Table IV are the middle values of the horizontal-axes. Error bars show standard error of the mean (SEM) with Bessel's correction for n = 3 simulations per data point.

2.3 Cofilin can resist spine head growth

In simulations, cofilin has a role in determining spine head size. Cofilin has previously been suggested as a key player in spine head growth ([42]). Whether increasing cofilin alone leads to spine size change remained to be seen. In column three of Fig. II, we find that increasing its levels, within a realistic biological range, in a spine head shrinks the spine head's size in 2D. Simulations here suggest that on the timescale of 20 seconds

Stubby spine head at 20.0 seconds: parameter sweep of η^q on CaMKIIβ against Arp2/3			
Membrane property / value type	q = 1 (n=3)	q = 2 (n=3)	q = 4 (n=3)
Aspect ratio / Jonckheere-Terpstra p-value	0.50	0.29	0.15
— / Pearson's correlation p-value	0.72	0.89	0.30
— / Pearson's correlation r-value	-0.048	0.018	-0.14
Perimeter / —	0.57	0.44	0.39
— / —	0.75	0.91	0.67
— / —	-0.042	0.015	-0.055
Enclosed area / —	0.47	0.38	0.33
— / —	0.62	0.81	0.56
— / —	-0.065	0.032	-0.077
Stubby spine head at 20.0 seconds: parameter sweep of η^q on Arp2/3 against CaMKIIβ			
Membrane property / value type	q = 1 (n=3)	q = 2 (n=3)	q = 4 (n=3)
Aspect ratio / Jonckheere-Terpstra p-value	—	**0.016**	0.18
— / Pearson's correlation p-value	—	0.091	0.24
— / Pearson's correlation r-value	—	0.22	-0.16
Perimeter / —	—	**0.045**	**0.0014**
— / —	—	0.30	**0.0033**
— / —	—	0.14	0.38
Enclosed area / —	—	**0.031**	**0.00069**
— / —	—	0.18	**0.0016**
— / —	—	0.17	0.41
Stubby spine head at 20.0 seconds: parameter sweep of η^q on cofilin against Arp2/3			
Membrane property / value type	q = 1 (n=3)	q = 2 (n=3)	q = 4 (n=3)
Aspect ratio / Jonckheere-Terpstra p-value	0.36	**0.013**	**0.045**
— / Pearson's correlation p-value	0.79	0.19	0.16
— / Pearson's correlation r-value	-0.035	-0.17	-0.18
Perimeter / —	0.18	0.25	**0.0050**
— / —	0.27	0.41	**0.024**
— / —	0.15	0.11	-0.29
Enclosed area / —	0.15	0.26	**0.0056**
— / —	0.26	0.39	**0.022**
— / —	0.15	0.12	-0.29

Table II: Statistical values for monotonicity and correlation in double parameter sweeps of CaMKIIβ and cofilin vs. Arp2/3 in stubby spine heads. Jonckheere-Terpstra p-values are calculated using "jonckheereTest" in the "PMCRPlus" package of the R programming language. Stubby statistical values match the format of the parameter sweep of Fig. III. Trend tests for monotonicity, p-values < 0.05 are bold under the Jonckheere 1-sided test, with sidedness determined by the sign of Pearson's r in a linear fit.

of a model for LTP, cofilin-dependent remodeling decreases size (p = 0.00030 for area; p = 0.00050 for perimeter; in Table I) for stubby spine heads. A likely reason for the decrease in size is that a filament bound with more cofilin has a weaker angular bending stiffness, which affects its ability to push against the membrane.

Previously, cofilin has been known to be necessary in order to shrink spine heads during long-term depression ([43]) and its inhibition conducive to spine head growth during long-term potentiation ([44, 45]). We find that it is indeed realistic behavior for cofilin to have such an effect during long-term potentiation in the stubby spine head. Stimulative augmentation of synthesis rates, i.e. from modeling glutamate uncaging, is

the implementation of long-term potentiation in our simulation. The simulation result is corroborative with previous research.

An effect of cofilin observed in simulations is to resist growth provided by Arp2/3 during LTP (p = 0.00030 for enclosed area; in Fig. II). The effect is not simply independent of Arp2/3 growth nor simply additive as demonstrated in Table II. Rather, despite cofilin having roughly greater correlation magnitude than Arp2/3 (Table I), i.e. around r = -0.33 for cofilin and around r = 0.22 for Arp2/3, applying $q = 2$ to cofilin, which is twice the nullification value of $q = 1$, does not overcompensate (p = 0.26, r = 0.12; in Table II) for Arp2/3 growth. Cofilin overcompensates for Arp2/3 growth actually at $q = 4$ (p = 0.0056, r = -0.29; in Table II). We observe that Arp2/3 does not completely mask the effect of cofilin induced shrinkage of spine head size, i.e. masking occurs only at $q \in \{1, 2\}$, but an effect of cofilin on spine head size (r = -0.29, p = 0.0056; in Table II) is recovered by $q = 4$. Arp2/3 has a conditional nullification on cofilin, based on roughly $q \leq 2$, log-ratio threshold between cofilin and Arp2/3 synthesis rates, pertaining to stubby spine head size. The effect from overactivating cofilin in shrinking spine head size is observed in biological experiment ([46]). The model we present here with Aip1 suggests that, being necessary for Aip1 binding, cofilin supports Aip1 mechanistically, but not synergistically for morphological size (r = -0.33, p = 0.00030 for cofilin; r = 0.45, p = 0.00048 for Aip1; in Table I), during LTP-like spine head growth.

We also present here a hypothesis for how opposite effects of cofilin and Aip1, both as part of the severing mechanism, on spine head size could work. Cofilin does not allow Arp2/3 to bind to locations where cofillin is bound on an actin filament. This competitive binding limits further action of cofilin-Aip1. Further binding of cofilin on the filaments that do exist weakens those filaments biomechanically by decreasing angular bending stiffness. According to this hypothesis, there exist a lesser number of filaments, and further amounts of cofilin weaken the working ability of actin filaments on growing the spine head membrane. This hypothetical mechanism would out-compete increase in binding locations for Aip1 (Eq. (24)) by quicker binding of cofilin to actin filaments (Eqs. (16, 17, 18)).

2.4 Cofilin as only actin filament severing mechanism leads to uncertainty in effects of ABPs

In this paper, we present two models, models with and without Aip1. In this subsection, we focus on the model without Aip1. Cofilin is the only molecule that can sever actin filaments through actin filament breaking (Eq. 23) in this model. In this model's parameter sweep (Fig. VI), Arp2/3 is the only ABP to significantly affect stubby spine head morphology, and it does so with a large r-value (r = 0.43, p = 0.0034; in Table III) compared to that of other ABPs (r = -0.11 for CaMKIIβ and r = 0.066 for cofilin; in Table III). In sections 2.1–2.3, all four ABPs (including Aip1) have significant effects on stubby spine head morphology. Therefore, Aip1 inclusion in the DGG model leads to less uncertainty about the effect of ABP mechanism on stubby spine head morphology. Inclusion of the Aip1 severing mechanism presented in [47] can lead to better certainty about other spine head morphology mechanisms. The reason is likely that the addition of the Aip1 binding-and-severing mechanism with a

severing event approximately every 0.7 s [48] for each bound Aip1 protein will generate more actin filaments than through biomechanical breaking alone. This increase in actin network size, will lead to a more biomechanically dynamic actin network that affects membrane morphology.

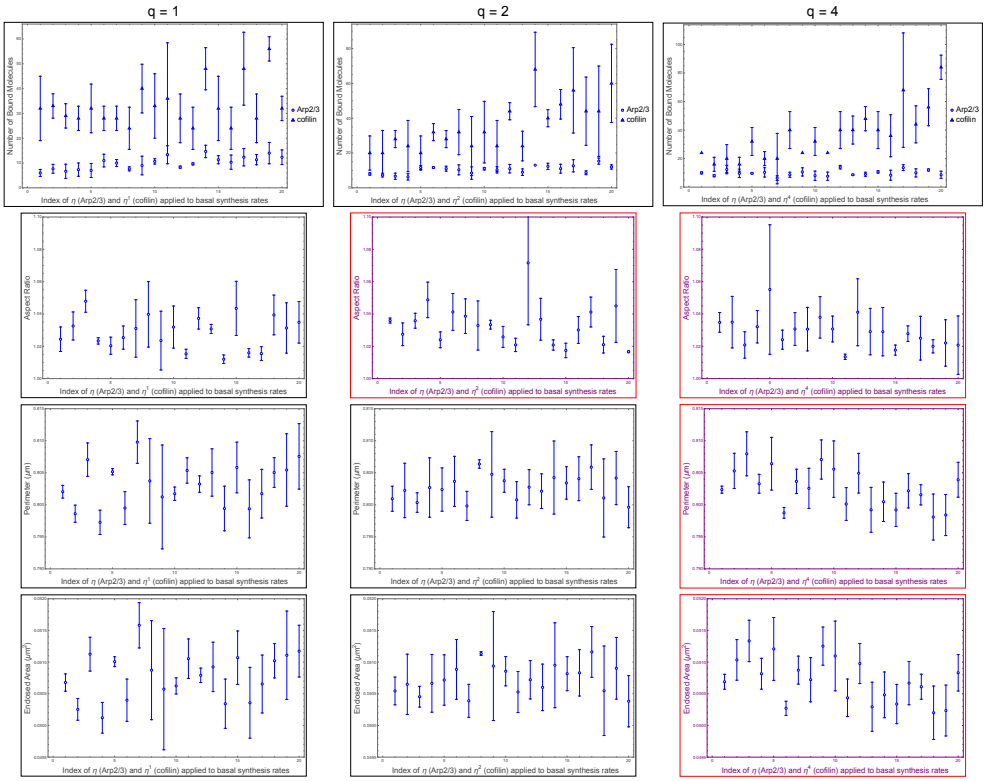

Fig. V: Interaction between Arp2/3 and cofilin in the stubby spine head: Dependence of membrane properties on synthesis rates of Arp2/3 and cofilin demonstrated in parameter sweeps. For a chosen value of η, it is sequentially multiplied or divided to the original, basal synthesis rates, but at different powers of η for Arp2/3 or cofilin, informed by the statistical values in Table I. η is directly applied to Arp2/3 synthesis, and η (first column), η^2 (middle column), and η^4 (last column) are applied to cofilin synthesis. The basal synthesis rates provided in Table IV are the middle values of the horizontal-axes. Error bars show standard error of the mean (SEM) with Bessel's correction for n = 3 simulations per data point. Indigo colored graphs are significant under p-value threshold 0.05. For the frames surrounding individual plots, blue is increasing trend, and red is decreasing trend.

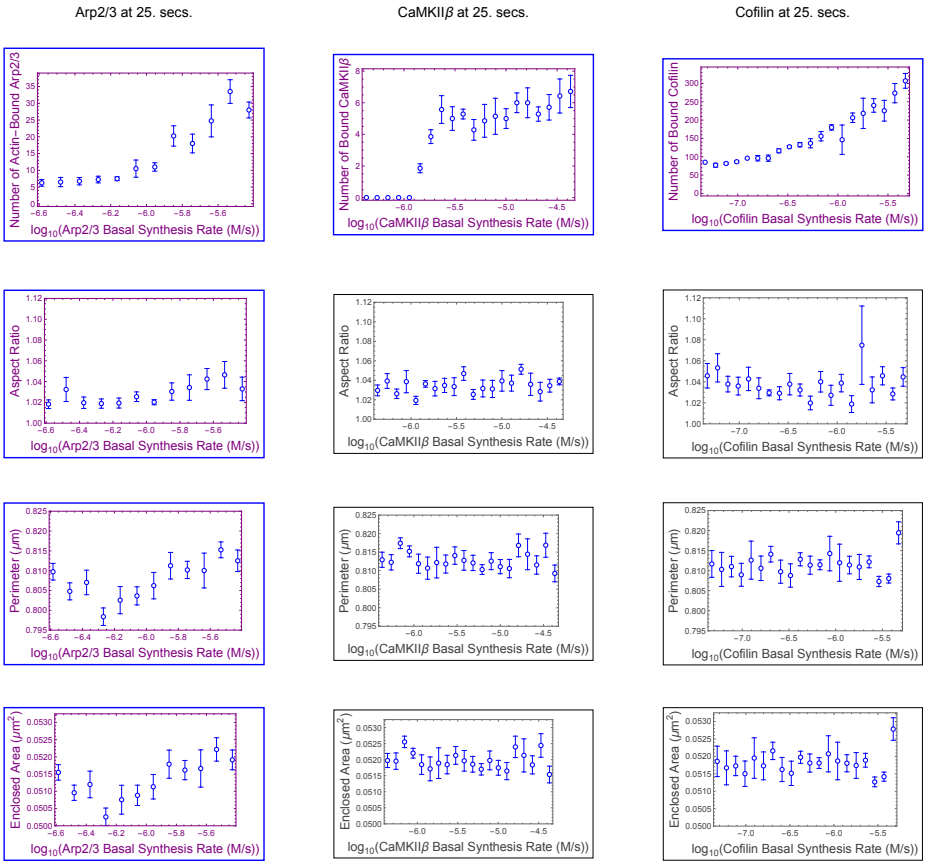

Fig. VI: Dependence of membrane properties on synthesis rates of three actin-binding regulatory proteins demonstrated in parameter sweeps. This model lacks the ABP Aip1 compared to the model in Fig. II. The basal synthesis rate provided in Section 4 Table IV is the middle value for CaMKIIβ and cofilin horizontal-axes. For Arp2/3 and Aip1, the range is truncated at the upper end of synthesis rate. Error bars show standard error of the mean (SEM) with Bessel's correction, for a number of stochastic simulations each. We calculate membrane aspect ratio, membrane perimeter, and membrane enclosed area for each simulation snapshot. The number of simulations is 4 for Arp2/3 and 5 for cofilin and for CaMKIIβ, corresponding to each mean value with error bar in the plots. Indigo graphs are significant under p-value threshold 0.05. For the frames surrounding significant individual plots, blue is a significant increasing trend, and red is a significant decreasing trend as determined by Table I. The range on log-scale for the parameter sweep consists of 10× smaller to at most 10× larger than the estimated, basal synthesis rates for CaMKIIβ and cofilin, with range truncated at the upper end for Arp2/3 and Aip1.

Stubby spine head at 25.0 seconds: parameter sweep of model without Aip1			
Membrane property / value type	Arp2/3 (n=4)	CaMKIIβ (n=5)	cofilin (n=5)
Aspect ratio / Jonckheere-Terpstra p-value	**0.0059**	0.16	0.18
— / Pearson's correlation p-value	**0.0048**	0.30	0.86
— / Pearson's correlation r-value	0.41	0.10	-0.018
Perimeter / —	**0.0065**	0.080	0.32
— / —	**0.0043**	0.35	0.47
— / —	0.41	-0.095	0.073
Enclosed area / —	**0.0034**	0.063	0.38
— / —	**0.0026**	0.29	0.51
— / —	0.43	-0.11	0.066

Table III: Statistical values for monotonicity and correlation in double parameter sweeps of CaMKIIβ and cofilin vs. Arp2/3 in stubby spine heads. Jonckheere-Terpstra p-values are calculated using "jonckheereTest" in the "PMCRPlus" package of the R programming language. Stubby statistical values match the format of the parameter sweep of Fig. III. Trend tests for monotonicity, p-values < 0.05 are bold under the Jonckheere 1-sided test, with sidedness determined by the sign of Pearson's r in a linear fit.

3 Methods

3.1 Coarse-graining of multiple actin monomers into single objects

As actin cytoskeleton grows or shrinks within the synaptic spine head, there is a continuing turnover of F-actin governed by different dynamics at the two different ends of a single filament, the barbed and pointed ends ([49]). The main processes that can occur in an actin network undergoing remodeling are elongation and retraction at the barbed end with rate parameters ($k_{\text{barbed, on}}$, $k_{\text{barbed, off}}$), elongation and retraction at the pointed end with rates ($k_{\text{pointed, on}}$, $k_{\text{pointed, off}}$), breaking from bending angles with parameters ($\theta_{\text{Break, Actin}}, \theta_{\text{Break, Cofilactin}}, \theta_{\text{Break, Boundary}}$), severing from Aip1 ($k_{\text{sever}}$), de-branching from cofilin ($k_{\text{de-branch}}$), capping ($k_{\text{cap, on}}, k_{\text{cap, off}}$), bundling and unbundling ($k_{\text{CaMKII}\beta\text{, on}}, k_{\text{CaMKII}\beta\text{, off}}$), and branch nucleation (k_{branch},k_{unbranch}) ([1]). These rate parameters are all in Table IV. We begin with rate constants found in literature and then compute the coarse-grained rate constants – replacing multiple actin monomers with 2D coordinates at their pointed end endpoints – for a more computationally efficient simulation. Using a coarse-grained model, we then simulate the dynamics of the actin cytoskeleton.

The barbed end of an actin filament adds monomers faster than the pointed end, which nets removal of monomers faster. Furthermore, the filament near the actin pointed end eventually forms more actin-ADP than near the barbed end, which retains newly added actin-ATP. These dynamics lead to directional pushing onto the membrane predominantly near clusters of barbed ends. To support this mechanism, the membrane-attached ends adaptively step, based on Brownian ratchet biophysics ([50]), their optimal coarse-graining length.

Coarse-graining is achieved by simulating aggregate rates and storing the binding numbers of attached molecules and the IDs of linked objects, for a total of 5–6 parameters per actin object. Below, in each DGG rule, just a relevant subset of parameters are displayed inside the $\langle\!\langle \ldots \rangle\!\rangle$ parentheses associated with objects.

Coarse-grained rate constants for polymerization are found by dividing the coarse-grained number into rates of elongations. The retraction, k^{-}_{barbed}, at a coarse-graining number is the rate for which every actin monomer, considering attached molecules, unbinds from the actin filament. Coarse-grained constants for retraction k^{-}_{barbed} that are dependent on the types of actin stored inside the object are computed as a rate divided by the coarse-graining number. Coarse-graining methods are approximate but can significantly address the scalability of an *in silico* model which we use here.

Biophysically, we set the coarse-grained resting length as the unit length of the system. Using the unit length in meters, we scale parameters involving distance units for numerical range in simulation. Furthermore, to define a bond strength parameter of the logitudinal potential, we equate the spring constant, which is the squared-potential curvature, with the equilibrium curvature of an anharmonic 12-6 Lennard-Jones (LJ) potential (Eq. (28)) below. ϵ_{LJ} is a parameter for well-depth or equivalently known as the bond dissocation energy. Here k_{s} is the experimentally measured actin spring constant, scaled as a series of springs from the original experimental measurement, into a single spring of distance between two adjacent monomers. To yield k_{s}, coarse-graining divides the original spring constant by the number of coarse-grained monomers, i.e. $k_{\text{s}}/N_{\text{CG}}$, in the equation defining ϵ_{LJ}. After ϵ_{LJ} for a single spring is estimated, this value is multiplied by N_{CG} to represent the total energy stored in the series of connections that comprises a single bond between objects in the scaled simulation. The angular bending constant is the flexural rigidity divided by the equilibrium length of a rod.

3.2 Actin cytoskeleton remodeling

Each of the main F-actin end types, barbed and pointed, can elongate or retract based on individual rate constants that also depend on type of bound nucleotide. ADP+Pi and ADP rate constants have been found to be experimentally similar, so for simplicity we equate them in our simulation.

To provide a better picture of how a rule functions, rules for actin polymerization and retraction are shown below. In the "with" clauses we have converted the rate constant to a function of species number and membrane area instead of concentration. $R(\theta)$ is a 2×2 rotation matrix with angle θ.

Actin Barbed End Elongation:

$$\begin{array}{ll} (\bigcirc_1 \longrightarrow \bullet_2) & \langle\!\langle\ (\boldsymbol{x}_1, \theta_1, \eta_1),\ (\boldsymbol{x}_2, \theta_2, \eta_2)\ \rangle\!\rangle \\ \longrightarrow (\bigcirc_1 \longrightarrow \bigcirc_2 \longrightarrow \bullet_3) & \langle\!\langle\ (\boldsymbol{x}_1, \theta_1, \eta_1),\ (\boldsymbol{x}_2, \theta_2, \eta_2),\ (\boldsymbol{x}_3, \theta_3, \eta_3)\ \rangle\!\rangle \end{array} \tag{5}$$

$$\textbf{with} \quad \frac{k_{\text{barbed, on, } \eta_3}}{N_{\text{CG}}}\ N_{\text{Actin, free}}$$

$$\begin{cases} \theta_2 \sim \mathcal{N}(0, \sigma_\theta = \sqrt{2/L_p})\ ; \\ \boldsymbol{x}_3 = \boldsymbol{x}_2 + R(\theta_2) \cdot (\boldsymbol{x}_2 - \boldsymbol{x}_1) \\ \eta_3 \in \{\text{ATP, ADP}\} \end{cases}$$

Here θ represents the middle angle between consecutive vectors of three nodes, which is zero for end nodes. The ";" represents sequential execution of two successive parameter assignments, so that θ_2 is sampled before use in setting $\boldsymbol{x}_3$. The sampling of θ_2 is centered around zero as its mean, with a standard deviation σ_θ taking into account the persistence length L_p. The topology and geometric parameters of an actin fiber are illustrated in Figure VIIa. As shown in the "where" clause in Eq. (5), η represents the type of nucleoside phosphate (one of ATP, ADP, or ADP+Pi) attached to the next new actin object, where we let ADP stand for both ADP and ADP+Pi due to similar rates of elongation and retraction. $\boldsymbol{x}, \theta$, and η, there are other actin object parameters to be introduced below, suppressed here for readability.

Node type symbols $\bigcirc$ and $\bullet$ represent interior and end segments of an actin filament, each segment being one or several actin units long depending on an adjustable coarse-graining parameter. Additional node type symbols include $\triangle$ for actin network branch point junction segments, $\blacktriangleright$ for end-capped actin segments, $\blacksquare$ for Arp2/3 proteins at branch points at the end of a new fiber, $\square$ for Arp2/3 proteins at branch points not at the end of a new fiber, and symbols $\bigcirc\!\!\!\!\bullet \in \{\bigcirc, \bullet, \blacktriangleright\}$, $\boxdot \in \{\blacksquare, \square\}$, $\bigstar \in \{\bigcirc, \bullet, \square, \blacksquare, \triangle, \blacktriangleright\}$ that each represent a choice among these basic symbols. We consider graph-local rewrite rules for cytoskeleton networks, and show how to derive DGG rules from a mutually exclusive and exhaustive collection of particular graph-local neighborhood types for the left hand sides of the rules, all from a global energy function that is a sum of graph-local terms.

The format of rule Eq. (5) above is similar to how it is implemented in Plenum with objects stored connected to one another in a graph, data stored within the objects such as position, angle, and nucleotide type, and clauses following the keyword "with" and "solving" to denote the propensity rule firing rate or differential equation respectively. The foregoing rule is presented as a mathematically idealized and "prettyprinted" version of its computational implementation in any specific piece of software. Executable rules in this paper were implemented in the Plenum package ([17]) for the Mathematica computer algebra and problem-solving environment. In Plenum the foregoing rule looks like Figure VIII.

From left to right, the parameters inside actin objects are an integer-valued object ID, spatial coordinates, an object ID "pointer" to the next actin object (for non-barbed end actin objects), the angle formed by the three objects, the angle formed with the branch (for junction objects), the type of bound molecule ATP, ADP, ADPPi, cofilin,

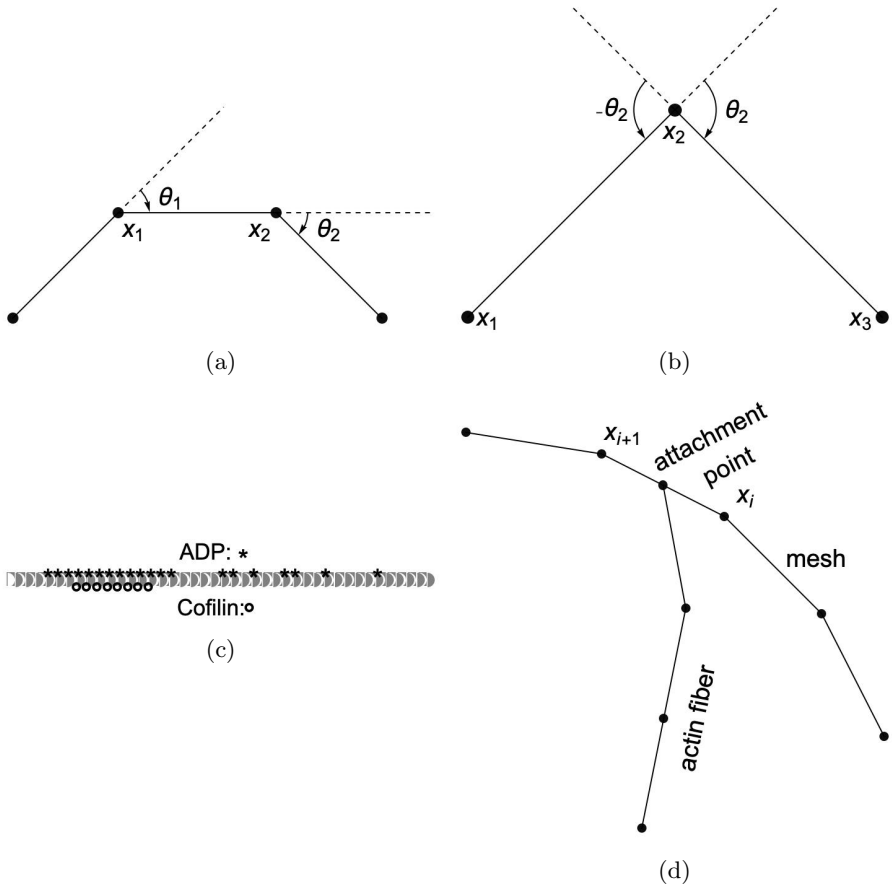

Fig. VII: Diagrammatic visualization of the physical system with (a) illustration of angle definitions, (b) providing opposite and equal angles with vectors, (c) visualizing an actin filament with ADP bound near cofilin boundaries, more toward the pointed end, as well as cofilin binding sequentially, and (d) depicting an actin fiber attached to a membrane mesh.

CaMKIIβ bound to the actin object, the spine vertex to which the end is bound, else a null pointer, (for end objects), and equilibrium length for the end object. The function "newpos" rotates a vector around the origin by an angle that is sampled by another function "grammarPDF", as in the additional clause of Eq. (5).

Similarly,

```
(*Rule for elongating a two node graph from free actin-ATP*)
{aP == actin[ID, coords, IDNext, ang, nucleotide],
  barbedEnd[IDNext, coordsNext, nucleotideNext, nullPointer, dist],
  newID[NID],
  actinATPCount[numActin],
  spineHeadArea[area], s1 == spine[sID, sCoord, sIDNext],
  s2 == spine[sIDNext, sCoordNext, sIDNextNext]}
  ->
  {actinATPCount[numActin - nCG],
  newID[NID + 1], aP,
  spineHeadArea[area],
  (* make the replacement node for the new INT: *)
  actin[IDNext, coordsNext, NID, randAng, nucleotideNext],
  (* make the newly created end node: *)
  barbedEnd[NID,
   If[pointSegmentDistance[coordsNext, sCoord, sCoordNext] <
     overgrowthL,
    raySegmentIntersection[coordsNext, coordsNext - coords, sCoord,
     sCoordNext],
    coordsNext +
     actinObjectRise newPos[coordsNext - coords, randAng]/
       Norm[coordsNext - coords]], ATP,
   If[pointSegmentDistance[coordsNext, sCoord, sCoordNext] <
     overgrowthL, sID, nullPointer], actinObjectRise], s1, s2
  },
with[kPlusBarbedT/nCG numActin*
  grammarPDF[NormalDistribution[0.0, \[Theta]p], randAng] Boole[
   numActin > nCG] Boole[
   rayIntersectsSegmentQ[coordsNext, coordsNext - coords, sCoord,
    sCoordNext]]]
```

Fig. VIII: Actual Plenum rule text corresponding to the rule of Eq. (5). Here, we make use of the sub-types to an "actin" general type, which includes the "barbedEnd[]" and "actin[]" headers. Sub-dividing types allow for a corpus of rules in the DGG ruleset that are compatible with a cognitive learning algorithm called "chunking" ([51]). Chunking involves sub-dividing a problem and storing solutions for future use. The casework leads to, in total, hundreds of DGG rules that efficiently contribute to simulation in the Plenum modeling language.

Actin Barbed End Retraction:

$$\begin{aligned} &(\bigcirc_1 \longrightarrow \bigcirc_2 \longrightarrow \bullet_3) && \langle\!\langle\ (\boldsymbol{x}_1,\, \theta_1,\, \eta_1),\, (\boldsymbol{x}_2,\, \theta_2,\, \eta_2),\, (\boldsymbol{x}_3, \theta_3,\, \eta_3)\ \rangle\!\rangle \\ \longrightarrow\ &(\bigcirc_1 \longrightarrow \bullet_2) && \langle\!\langle\ (\boldsymbol{x}_1,\, \theta_1,\, \eta_1),\, (\boldsymbol{x}_2,\, \theta_2,\, \eta_2)\ \rangle\!\rangle \end{aligned} \tag{6}$$

$$\textbf{with} \quad \frac{k_{\text{barbed, off, }\eta_3}}{N_{\text{CG}}}\, N_{\text{Actin, free}}$$

In addition there are two further cases of the foregoing two rules with different context nodes ($\square_1$ and $\triangle_1$ in addition to $\bigcirc_1$), i.e. nodes that remain unchanged in rule firing, like enzymes in a catalysed chemical reaction. Pairing the foregoing two rules together with the $\rightleftharpoons$ bidirectional arrow, and omitting the propensity functions, these cases are:

Actin Barbed End Elongation:

$$\begin{array}{ll} (\square_1 \longrightarrow \bullet_2) & \langle\!\langle\ (\boldsymbol{x}_1, \theta_1, \eta_1),\ (\boldsymbol{x}_2, \theta_2, \eta_2)\ \rangle\!\rangle \\ \rightleftharpoons\ (\square_1 \longrightarrow \bigcirc_2 \longrightarrow \bullet_3) & \langle\!\langle\ (\boldsymbol{x}_1, \theta_1, \eta_1),\ (\boldsymbol{x}_2, \theta_2, \eta_2),\ (\boldsymbol{x}_3, \theta_3, \eta_3)\ \rangle\!\rangle \end{array} \tag{7}$$

and

Actin Barbed End Elongation:

$$\begin{array}{ll} (\triangle_1 \longrightarrow \blacksquare_2) & \langle\!\langle\ (\boldsymbol{x}_1, \theta_1, \eta_1),\ (\boldsymbol{x}_2, \theta_2, \eta_2)\ \rangle\!\rangle \\ \rightleftharpoons\ (\triangle_1 \longrightarrow \square_2 \longrightarrow \bullet_3) & \langle\!\langle\ (\boldsymbol{x}_1, \theta_1, \eta_1),\ (\boldsymbol{x}_2, \theta_2, \eta_2),\ (\boldsymbol{x}_3, \theta_3, \eta_3)\ \rangle\!\rangle \end{array} \tag{8}$$

For each of these barbed end elongation/retraction rules there is a corresponding pointed end rule. The first two are shown below.

Actin Pointed End Elongation:

$$\begin{array}{ll} (\bullet_2 \longrightarrow \bigcirc_3) & \langle\!\langle\ (\boldsymbol{x}_2, \theta_2, \eta_2),\ (\boldsymbol{x}_3, \theta_3, \eta_3)\ \rangle\!\rangle \\ \rightleftharpoons\ (\bullet_1 \longrightarrow \bigcirc_2 \longrightarrow \bigcirc_3) & \langle\!\langle\ (\boldsymbol{x}_1, \theta_1, \eta_1),\ (\boldsymbol{x}_2, \theta_2, \eta_2),\ (\boldsymbol{x}_3, \theta_3, \eta_3)\ \rangle\!\rangle \end{array} \tag{9}$$

$$\textbf{with}\quad \frac{k_{\text{pointed},\eta_3}}{N_{\text{CG}}}\ N_{\text{Actin, free}}$$
$$\begin{cases} \theta_2 \sim \mathcal{N}(0, \sigma_\theta)\ ; \\ \boldsymbol{x}_1 := \boldsymbol{x}_2 + R(-\theta_2) \cdot (\boldsymbol{x}_2 - \boldsymbol{x}_3) \\ \eta_1 \in \{\text{ATP, ADP}\} \end{cases}$$

Actin Pointed End Retraction:

$$\begin{array}{ll} (\bullet_1 \longrightarrow \bigcirc_2 \longrightarrow \bigcirc_3) & \langle\!\langle\ (\boldsymbol{x}_1, \theta_1, \eta_1),\ (\boldsymbol{x}_2, \theta_2, \eta_2),\ (\boldsymbol{x}_3, \theta_3, \eta_3)\ \rangle\!\rangle \\ \rightleftharpoons\ (\bullet_2 \longrightarrow \bigcirc_3) & \langle\!\langle\ (\boldsymbol{x}_2, \theta_2, \eta_2),\ (\boldsymbol{x}_3, \theta_3, \eta_3)\ \rangle\!\rangle \end{array} \tag{10}$$

$$\textbf{with}\quad \frac{k_{\text{pointed},\eta_1}}{N_{\text{CG}}}\ N_{\text{Actin, free}}$$

We again have that $\sigma_\theta = \sqrt{\frac{2}{L_p}}$, where L_p is persistence length transformed to unit length of an actin filament segment, according to the statistics of a semiflexible polymer and a random walk in small angles. Note that angle θ_2 is being used in the reverse direction of traversal along the fiber, and hence has its sign reversed, as shown in Fig. VIIb. This specification is also used to update the angles in the

direct neighborhood of the center node, after moving it. Thus, angles are accessed for potential severing and not recomputed at each simulation iteration.

In addition to end elongation and retraction, there exist several more rule types for network remodeling such as:

1. Ordinary differential equation (ODE) molecule rules for synthesis and degradation

   Basal and stimulated (e.g., influx) synthesis rates for simulated proteins are estimated from experimental data as done previously ([13]). As in [13], the following differential equation estimates the experimental system which provides the data:

$$\frac{dM}{dt} = I_{S,M} + I_M - k_M M, \tag{11}$$

   where M is the molecule's normalized fluorescence measurement, I represents the influxes from stimuli ($I_{S,M}$) and basal rates (I_M) respectively, and k_M is the degradation. For each molecule of interest, we fit the curves in [32] to differential equation Eq. (11) above. The results for CaMKIIβ (bundling) and Arp2/3 are shown in Figure IX comparing the experimental data trend with the parameter fitting. The resulting estimated rates are provided in Table 1. We set the initial number of proteins at the steady-state concentrations provided by basal synthesis rates. The combined basal and stimulation rates create actin and ABPs (cofilin, Arp2/3, CaMKIIβ, Aip1), simulating LTP induction, as in [32] and [13].

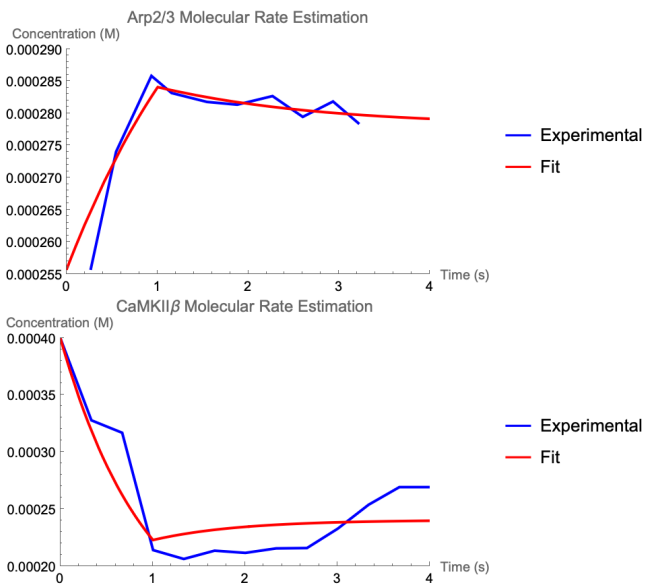

Fig. IX: In the top plot, the estimation of Arp2/3 synthesis, influx, and degradation rates from experimental data ([32]) are shown, and in the bottom plot, those for CaMKIIβ, a bundling protein, are shown. Standard errors in estimated rates are shown in Table IV.

2. Stochastic rules for post-polymerization phosphate release

   The stochastic rules for phosphate release follow actin-attached nucleotide state transitions that regulate binding and unbinding of cofilin in addition to actin polymerizing dynamics. Thus, these stochastic rules regulate cytoskeletal remodeling propensities like synthesis and degradation ODE rules. Phosphate release occurs sequentially from ATP to ADP+Pi and from ADP+Pi to ADP. ADP+Pi is an intermediate state, where the inorganic phosphate (Pi) is mainly bound to the actin filament and not to the nucleotide molecule ([52]). Adjacent cofilin molecules bound to the actin filament accelerate the release of Pi from actin-ADP+Pi to yield actin-ADP.
3. Branching by Arp2/3 nucleation which forms a junction with three objects connected to a single object node with an expected angle of around 70°= $\frac{70\pi}{180}$radians.

   Actin Arp2/3 Branching:

$$\begin{array}{l} \left(\begin{array}{ccccc} \bigcirc_1 & \longrightarrow & \bigcirc_2 & \longrightarrow & \bigcirc_3 \\ & & \blacksquare_4 & & \end{array}\right) \\ \longrightarrow \left(\begin{array}{ccccc} \bigcirc_1 & \longrightarrow & \blacktriangle_2 & \longrightarrow & \bigcirc_3 \\ & & & \searrow & \\ & & & & \blacksquare_4 \end{array}\right) \end{array} \quad \begin{array}{l} \langle\!\langle\ (\boldsymbol{x}_1),\ (\boldsymbol{x}_2,\ \eta_2),\ (\boldsymbol{x}_3),\ (\boldsymbol{x}_4)\ \rangle\!\rangle \\ \langle\!\langle\ (\boldsymbol{x}_1),\ (\boldsymbol{x}_2,\ \eta_2,\ \theta),\ (\boldsymbol{x}_3),\ (\boldsymbol{x}_4)\ \rangle\!\rangle \end{array} \tag{12}$$

   with $k_{\text{branch}}\ N_{\text{Arp, free}}\ (1-\delta(\eta_2, \text{cof}))$

$$\begin{cases} \text{s} \sim \mathcal{U}(\pm 1)\ ; \\ \theta \sim \mathcal{N}(\frac{70\pi}{180}\text{s}, \sigma_\theta)\ ; \\ \boldsymbol{x}_4 := \boldsymbol{x}_2 + R(\theta_2)\cdot(\boldsymbol{x}_2 - \boldsymbol{x}_1) \end{cases}$$

   Here, the branching mechanism is mutually exclusive with already bound cofilin.

   Actin Arp2/3 Unbranching:

$$\begin{array}{l} \left(\begin{array}{ccccc} \bigcirc_1 & \longrightarrow & \blacktriangle_2 & \longrightarrow & \bigcirc_3 \\ & & & \searrow & \\ & & & & \blacksquare_4 \end{array}\right) \\ \longrightarrow (\bigcirc_1 \longrightarrow \bigcirc_2 \longrightarrow \bigcirc_3) \end{array} \quad \begin{array}{l} \langle\!\langle\ (\boldsymbol{x}_1, \theta_1),\ (\boldsymbol{x}_2, \theta_2),\ (\boldsymbol{x}_3, \theta_3)\ \rangle\!\rangle \\ \langle\!\langle\ (\boldsymbol{x}_1, \theta_1),\ (\boldsymbol{x}_2, \theta_2),\ (\boldsymbol{x}_3, \theta_3),\ (\boldsymbol{x}_4, \theta_4)\ \rangle\!\rangle \end{array} \tag{13}$$

   with k_{unbranch}

   k_{unbranch} is accelerated by a factor of roughly 50 in the case that cofilin is bound to the junction (black triangle) node.
4. Capping, which stops the barbed end from elongating or retracting until the cap is removed, and uncapping:

   Actin Barbed End Capping:

$$\begin{array}{l} (\bullet_1) \\ \longrightarrow (\blacktriangleright_1) \end{array} \quad \begin{array}{l} \langle\!\langle\ (\boldsymbol{x}_1, \theta_1)\ \rangle\!\rangle \\ \langle\!\langle\ (\boldsymbol{x}_1, \theta_1)\ \rangle\!\rangle \end{array} \tag{14}$$

   with $k_{\text{cap, on}}\ N_{\text{Cap, Free}}$

Actin Barbed End Uncapping:

$$\begin{array}{ll} (\blacktriangleright_1) & \langle\!\langle\ (\boldsymbol{x}_1, \eta_{1,\ \mathrm{Aip1}})\ \rangle\!\rangle \\ \longrightarrow (\bullet_1) & \langle\!\langle\ (\boldsymbol{x}_1, \eta_{1,\ \mathrm{cof}})\ \rangle\!\rangle \end{array} \tag{15}$$

with $k_{\mathrm{cap,\ off}}$

5. Cofilin binding, which weakens bending stiffness of bound segments called cofilactin, and lowers the minimal angle for severing at boundaries along the actin filament (under the rule of Eq. (23) below). These rules require that further actin parameters η_* be deployed:

Accelerated Cofilin Binding (2-Node):

$$\begin{array}{ll} (\{\bigstar_1 \longrightarrow \{\bigstar\backslash\boxdot\}_2) & \langle\!\langle\ (\boldsymbol{x}_1, \mathrm{cof}),\ (\boldsymbol{x}_2, \mathrm{ADP})\ \rangle\!\rangle \\ \longrightarrow (\{\bigstar_1 \longrightarrow \{\bigstar\backslash\boxdot\}_2) & \langle\!\langle\ (\boldsymbol{x}_1, \mathrm{cof}),\ (\boldsymbol{x}_2, \mathrm{cof})\ \rangle\!\rangle \end{array} \tag{16}$$

with $\frac{k_{\mathrm{on\text{-}edge,\ cofilin}}}{N_{\mathrm{CG}}} N_{\mathrm{cofilin,\ Free}}$

Here ADP indicates the nucleotides attached to filament segment object i are fully in an ADP state and "cof" indicates the attached molecules are in a cofilin bound state, as illustrated in Fig. VIIc.

This rule exists with its flipped version with cofilin binding from the right node to the left node towards the pointed end.

Accelerated Cofilin Binding (1-Node):

$$\begin{array}{ll} (\{\bigstar\backslash\boxdot\}_2) & \langle\!\langle\ (\boldsymbol{x}_1, \text{cof-S}),\ \rangle\!\rangle \\ \longrightarrow (\{\bigstar\backslash\boxdot\}_2) & \langle\!\langle\ (\boldsymbol{x}_1, \mathrm{cof})\ \rangle\!\rangle \end{array} \tag{17}$$

with $\frac{2k_{\mathrm{on\text{-}edge,\ cofilin}}}{N_{\mathrm{CG}}} N_{\mathrm{cofilin,\ Free}}$

This rule starts with matching "cof-S" which is a single bound cofilin, as the result of a rare event in Eq. (16), and converts to "cof" to represent the whole node bound with cofilin. In an actin helix, a singly bound cofilin can cooperatively ([53]) add adjacently to the edge of a cofilin segment in available directions, i.e. left-right leads to ×2 in the above "with" clause.

Bare Filament Cofilin Binding:

$$(\{\bigstar\backslash\boxdot\}_1)\,\langle\!\langle(\boldsymbol{x}_1, \mathrm{ADP})\rangle\!\rangle \longrightarrow (\{\bigstar\backslash\boxdot\}_1)\,\langle\!\langle(\boldsymbol{x}_1, \text{cof-S})\rangle\!\rangle \tag{18}$$

with $k_{\mathrm{on\text{-}single,\ cofilin}} N_{\mathrm{cofilin,free}}$

Actin Filament Cofilin Unbinding:

$$(\bigstar_1)\,\langle\!\langle (\boldsymbol{x}_1, \mathrm{cof}) \rangle\!\rangle \longrightarrow (\bigstar_1)\,\langle\!\langle (\boldsymbol{x}_1, \mathrm{ADP}) \rangle\!\rangle \tag{19}$$

with $\frac{k_{\text{off-edge, cofilin}}}{N_{\mathrm{CG}}}$

6. Bundling, which creates another junction type with a CaMKIIβ object connected to two actin objects that are not already connected to each other:

Actin Filament CaMKIIβ Binding:

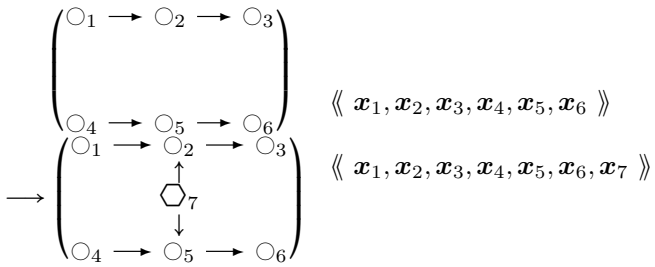

(20)

with $k_{\text{on, Bundling}} N_{\mathrm{Cam}} \mathcal{H}\left(\mathcal{D}_{\mathcal{U}} - \|x_2 - x_5\|\right) \mathcal{H}\left(\theta_{\mathrm{Bundle}} - \cos^{-1}\left(\frac{(x_3 - x_1)\cdot(x_6 - x_4)}{\|x_3 - x_1\|\|x_6 - x_4\|}\right)\right)$

where $\mathcal{D}_{\mathcal{U}}$ and θ_{Bundle} are maximal numerical values of distance and angle for coarse-grained binding of CaMKIIβ, and where we denote the Heaviside function as

$$\mathcal{H}(x) = \begin{cases} 1 & x \geq 0 \\ 0 & x < 0 \end{cases}$$

The reverse process is given by this rule:

Actin Filament CaMKIIβ Unbinding:

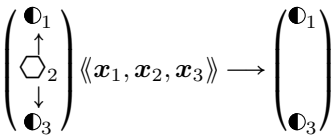

with $k_{\text{off, Bundling}}$ (21)

7. Filament breaking, from the action of cofilin or aip1.

Actin Filament De-Branching:

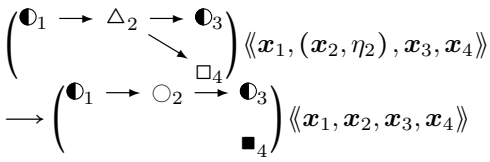

(22)

with $k_{\mathrm{debranch}} \exp\left(\delta\left(\eta_2, \mathrm{Cof}\right)\left(\sigma_{\mathrm{comp}} + k_{\mathrm{comp}}\right)\right)$

where k_{debranch} is the rate at which Arp2/3 naturally dissociates from a parent actin filament, σ_{comp} is the rate of increase from cofilin co-occupying a space on the actin filament that Arp2/3 does, and k_{comp} is the effect of strain and twist accelerating Arp2/3 dissociation due to cofilin binding at near-neighboring spots alonng the actin filament ([54]). Together, σ_{comp} and k_{comp} increase the rate of branching by roughly a factor of 50 ([54]).

Actin Filament Breaking:

$$\begin{aligned} &(\bigcirc_1 \longrightarrow \bigcirc_2) && \langle\!\langle\ (\boldsymbol{x}_1, \theta_1, \eta_{1,\ \text{Cofilin}}),\ (\boldsymbol{x}_2, \theta_2, \eta_{2,\ \text{Cofilin}})\ \rangle\!\rangle \\ \longrightarrow\ &(\bullet_1 \qquad \bullet_2) && \langle\!\langle\ (\boldsymbol{x}_1, \theta_1, \eta_{1,\ \text{Cofilin}}),\ (\boldsymbol{x}_2, \theta_2, \eta_{2,\ \text{Cofilin}})\ \rangle\!\rangle \end{aligned} \tag{23}$$

$$\begin{aligned} \textbf{with}\quad & k_{\text{biomech}} \max(\mathcal{H}(|\theta_1| - \theta_{\text{Actin}})(1 - \delta(\eta_1, \text{cof})) \\ & \mathcal{H}(|\theta_2| - \theta_{\text{Actin}})(1 - \delta(\eta_2, \text{cof})), \\ & \mathcal{H}(|\theta_1| - \theta_{\text{Boundary}})(1 - \delta(\eta_1, \text{cof})) \\ & \mathcal{H}(|\theta_2| - \theta_{\text{Boundary}})\delta(\eta_2, \text{cof}), \\ & \mathcal{H}(|\theta_1| - \theta_{\text{Boundary}})\delta(\eta_1, \text{cof}) \\ & \mathcal{H}(|\theta_2| - \theta_{\text{Boundary}})(1 - \delta(\eta_2, \text{cof}), \\ & \mathcal{H}(|\theta_1| - \theta_{\text{Cofilactin}})\delta(\eta_1, \text{cof}) \\ & \mathcal{H}(|\theta_2| - \theta_{\text{Cofilactin}})\delta(\eta_2, \text{cof})) \end{aligned}$$

This maximum (equivalent to a logical disjunction i.e. "or" operation) of Heaviside functions conditions actin filament breaking on three critical breaking angles dependent on the state of molecules bound to the coarse-grained object's actin monomers. The actin breaking angle is used for zero cofilin states within bound molecules, the cofilactin breaking angle is used for internal actins which have cofilin bound molecules, and the boundary breaking angle is used elsewhere where adjacent actin objects have different occupancies of cofilin molecules, hence indicating a cofilactin-actin boundary.

Aip1 Binding:

$$\begin{aligned} &(\bigcirc_1) && \langle\!\langle\ (\boldsymbol{x}_1, \theta_1, \eta_{1,\ \text{cof}}),\ \rangle\!\rangle \\ \longrightarrow\ &(\bigcirc_1) && \langle\!\langle\ (\boldsymbol{x}_1, \theta_1, \eta_{1,\ \text{Aip1}})\ \rangle\!\rangle \end{aligned} \tag{24}$$

$$\textbf{with}\quad k_{\text{on, Aip1}}$$

Actin Filament Severing:

$$\begin{aligned} &(\bigcirc_1 \longrightarrow \bigcirc_2) && \langle\!\langle\ (\boldsymbol{x}_1, \theta_1, \eta_{1,\ \text{Aip1}}),\ (\boldsymbol{x}_2, \theta_2, \eta_2)\ \rangle\!\rangle \\ \longrightarrow\ &(\blacktriangleright_1 \qquad \bullet_2) && \langle\!\langle\ (\boldsymbol{x}_1, \theta_1, \eta_{1,\ \text{Aip1}}),\ (\boldsymbol{x}_2, \theta_2, \eta_2)\ \rangle\!\rangle \end{aligned} \tag{25}$$

$$\textbf{with}\quad k_{\text{sever}}$$

Together, these rules lead to a treadmilling effect with turnover of actin monomers when the actin network is sufficiently large. The network preferentially moves outward in the direction of the barbed ends since the barbed end elongation rates are faster than the pointed end elongation rates. while the nodes toward the pointed ends are

eventually depolymerized. In this way it was originally proposed by theorists such as Mogilner and Oster that actin can provide a force to cellular compartments by interacting with their membranes ([20]). Considering Newtonian reactive forces of membrane on fiber and fiber on fiber, actin can also generate other forces within the compartment, leading to internal reorganization and deformation. The mechanism with which the actin network achieves moving the membrane along with its own fibers is the subject of the next section.

3.3 Biomolecular mechanisms of actin-binding proteins

Based on the foregoing rules, we summarize in this section the workings of each ABP in the context of actin filament network remodeling and biophysics.

3.3.1 Actin

The polymerization and depolymerization of actin are the driving mechanisms for actin dynamics in this model. In addition, a filament sub-graph that includes long rods causes an electrostatic disconnection between two adjacent actin objects as the objects exert only small radial forces on each other. The adjacency of the actin objects has its connection broken to create two new filaments (Eq. (23)).

3.3.2 Arp2/3

A junction object nucleates the Arp2/3 branch as a new filament with a pointed end. Arp2/3 can unbind and de-branch spontaneously, and encouraged by nearby bound cofilin ([54]).

3.3.3 Cofilin

The cofilin mechanism includes a slow binding to an unoccupied cofilin site on an actin protein within a coarse-grained actin object, which is independent of the state of the site's neighbors on an actin filament. There also is a faster binding, accelerated by the state of the site's neighbors ([53, 55]). Each bound site is mechanically weakened by a factor of five, as cofilin is known to weaken the bending stiffness of actin filaments ([56]). Nearby cofilin-bound sites accelerate the actin-bound ATP/ADP dynamics of neighboring sites.

Cofilin, when present in high numbers, destabilizes the filament by lowering bending stiffness, and causes breaking (Eq. (23)). Cofilin binding to an empty site on an actin filament is slow; however, each bound cofilin encourages (Eq. (16)) binding of cofilin to adjacent locations along the filament. Cofilin also facilitates the release of ADP+Pi to ADP ([57]) when it is present near to the actin monomer and facilitates breaking along interfaces ([55]) between cofilin-bound segments and non-bound segments. These mechanisms are implemented in our simulations with bound ATP/ADP and cofilin stored as values in actin object nodes (Eqs. (16-19)).

Cofilin competes with Arp2/3 for spots on an actin filament and facilitates the dissociation of a daughter branch from a parent filament ([54]). This is due to steric hindrance of the Arp2/3 molecule and also by altering the biophysics (e.g. twist ([58])) of the actin filament after cofilin binds.

Furthermore, cofilin creates a boundary angle regime for filament breaking, which subsequently occurs at a much smaller angle than cofilin-unbound segments ([59]). This is hypothesized to occur, in part, due to cofilin segments having a 5-fold weaker bending modulus than the unbound segments. Correspondingly, the bending modulus is weakened in simulation, by that factor, conditioned on bound cofilin.

3.3.4 Aip1

Aip1 has been known to accelerate severing of filaments ([48]). We implement the mechanism of Aip1 as a cofilactin (cofilin-bound actin) binding molecule with a severing mechanism in addition to that of cofilin ([47]), with a rate constant from [48]. After severing occurs, a barbed end capped by Aip1 is created ([47]), that can dissociate from the cofilactin barbed end to allow barbed end elongation, as well as a new pointed end.

3.3.5 CaMKIIβ

Filaments that are within a specified distance and angle of each other have a non-zero rate of binding by CaMKIIβ which links them with the the actin biophysics described in section 3.5 below. This includes the anisotropic buckling force and the bending force, together with their respective thermal Hessians. A biologically realistic equilibrium length between the filaments is kept as the uniform, optimal length until the bundling molecule unbinds.

3.4 Spine head morphodynamics

Dynamical Graph Grammars (DGGs) provide a well-defined way to accommodate dynamically changing system structure such as active cytoskeleton represented using dynamic graphs within nonequilibrium statistical physics as defined by the master equation. Such structure changes operate naturally at a coarser spatial scale than the force exertion of fixed topology objects on one another in biophysical kinetics. To obtain multiscale models then it is necessary to unify the two perspectives - grammar-defined discrete state changes and finer-scale biophysics - with specialized DGG kinetics rules that obey biophysical constraints such as Galilean invariance, conservation of momentum, and dissipation of conserved global energy.

In our model the spine head area grows, starting from an area that encloses a starting pair of actin objects. The mechanism of actin-membrane mutual growth is the attachment of actin objects to the membrane mesh as soon as they intersect, allowing propulsive force onto the membrane, Newtonian reactive force onto the actin network, and pressure onto the actin network. The entire model takes place in two dimensions (viewing the dendritic spine head from the top), due to our current computational limitations, although future work will aim at three dimensions. The requisite dynamics conditions for the implementation details are provided below.

First, actin rods intersecting through a pseudo-extended actin overgrowth length ([27]) with a spine head membrane rod have the end attached to the spine head membrane rod through the creation of a new spine head membrane vertex at that Cartesian coordinate. Second, the membrane is allowed to fluctuate from the curvature

energy term. The Helfrich energy mean curvature energy is given by:

$$E_H = \frac{\kappa}{2} \int_S (2H)^2 \, dA$$

To discretize this term for a 2D membrane polygon, we approximate the mean curvature H at each vertex $\mathbf{r}_i$. Let $\mathbf{r}_{i-2}$, $\mathbf{r}_{i-1}$, $\mathbf{r}_{i+1}$, $\mathbf{r}_{i+2}$ be the neighboring vertices of $\mathbf{r}_i$. Using the adjacent neighbors, we take the derivative of the unit tangent vector with respect to the arc length $\bar{w}$, which yields

$$H_{\Gamma(x_a,x_b,x_c)} = \left\| \frac{d\mathbf{T}}{d\bar{w}} \right\|, \tag{26}$$

where we approximate

$$\frac{dT^i}{d\bar{w}^i} \simeq \frac{1}{z^i} \left(\frac{x_1^{i+1} - x_1^i}{v^{i+1}} - \frac{x_1^i - x_1^{i-1}}{v^i}, \frac{x_2^{i+1} - x_2^i}{v^{i+1}} - \frac{x_2^i - x_2^{i-1}}{v^i} \right), \tag{27}$$

and $v^i = \|x^i - x^{i-1}\|$ and $z^i = \frac{v^i + v^{i+1}}{2}$. This scheme was presented in [18] (Supplementary Material), and when followed, leads to the update as follows: where $g^i = \left\| \frac{x^{i+1} - x^i}{v^i} - \frac{x^i - x^{i-1}}{v^{i-1}} \right\|^2$, we have that $H_{\Gamma(x_a,x_b,x_c,x_d,x_e)} = \frac{\sqrt{g^{i-1}}}{z^{i-1}} + \frac{\sqrt{g^i}}{z^i} + \frac{\sqrt{g^{i+1}}}{z^{i+1}}$.

The actin end is allowed to interpolate from the spine head membrane after polymerizing and extending beyond the overgrowth threshold length for the overgrowth dynamics, which follows the Brownian ratchet polymerization mechanism ([50]). An interpolating membrane mesh is maintained that imparts actin-end forces onto the vertices through attachment objects connecting actin ends to particular membrane rodsas in Figure VIId.

3.5 Actin network biophysics

The gradient descent rules below together comprise a stochastic first order Euler update for solving the force balance system of differential equations. It is analogous to stochastic gradient descent. These rules have a parameter k_{kinetic} which in the infinite limit recovers the ODE exactly. Alternatively we could have coded ODEs in the DGG, but we think that would be less efficient in the presence of substantial thermal noise.

There are two sub-sectors to our implemented biophysics sector: (1) pairwise forces due to energy terms coupling two adjacent segments or proteins of a polymer (and which subserve a fiber buckling process), and (2) three-node forces that act specifically on fiber bending angles. For each of these kinds of forces, there are several rules that update position according to the force. There is also a corresponding energy term whose negative spatial derivative is the force, and another kind of rule that implements Hessian Boltzmann sampling which represents thermal noise fluctuations.

To ensure that even dissipative biophysics is compatible with conservation of energy, the DGG kinetic rules must all be derivable from a single global energy function. This function will be a sum of two-object and three-object potential energy

functions. The three-object potential energies will be a function of the bending angle between three consecutive graph-connected filament segments, hence invariant to the Euclidean group of global translations and rotations. The two-object potential energies will be a function of the distance between the centroids of two graph-connected objects, hence also Euclidean-invariant.

The longitudinal pairwise energy $U_{\text{sep}}(x_1, x_2) = U_{\text{sep}}(r)$, where r is the separation distance $r = \|x_1 - x_2\|_2$ between two connected filaments segments (which could be a small as individual actin proteins), is standardly assumed to have a minimum-energy distance $r_{\min}$, to increase for larger distances and asymptote from below to a value of zero energy, and to increase rapidly to infinity as the segment-segment pairwise distance drops to zero - the repulsive core of the central force law. For example, this intermolecular potiential energy can be taken to be the LJ potential:

$$\hat{U}_{\text{LJ}}(x_1, x_2) = \hat{U}_{\text{LJ}}(\|x_1 - x_2\|_2) = \epsilon_{\text{LJ}} \left(\left(\frac{\sigma_{\text{LJ}}}{\|x_1 - x_2\|} \right)^{12} - \left(\frac{\sigma_{\text{LJ}}}{\|x_1 - x_2\|} \right)^{6} \right). \tag{28}$$

This potential takes its minimum value at $r = r_{\min}$. We will use this popular default choice, though there is no particular reason that actin proteins should have this potential energy law rather than one of many others that have similar properties.

This kind of potential smoothly "breaks" the connection between two segments for large r, since an energy constant with respect to position implies zero force. Thus two sufficiently distant segments could trigger a filament-breaking rule such as Eq. (23).

When such a model is applied to three successive points in a fiber, the result is a tri-nodal potential in which a buckling effect arises whereby under compression the middle filament node pushes away from the co-linear state. The relevant energy combination is:

$$U_{\text{tri-nodal,sep}}(x_1, x_2, x_3) = \tilde{U}_{\text{sep}}(x_1, x_2) + \tilde{U}_{\text{sep}}(x_2, x_3) \tag{29}$$

For an unbranched interior actin node in a filament at position x_2, the gradient of this energy equals the gradient of the globally summed U_{sep} over all connected pairs. There is a numerical reason to use the trinodal potential rather than the pairwise potential in the main DGG rule for buckling. For a nearly straight fiber, the gradients of the two pairwise potentials in which a given interior (non-boundary) node participates nearly cancel out. This cancellation is more efficiently achieved by an exact analytic vector sum in the gradient calculation of the trinodal potential, than by the stochastic addition of displacements resulting from the stochastic firing of a pairwise DGG rule on randomly chosen nodes which will eventually converge to the same stochastic cancellation on average.

Also for numerical reasons, we introduce a force-clipping two-body potential energy function that is used to ensure that the movements of the actin objects smoothly update towards a system minimum. The force-clipping is important because we are using a potential energy function $\hat{U}(r)$ for interparticle distance $r = \|x_1 - x_2\|$, such as the LJ potential $\hat{U}_{LJ}(r)$, that includes a strong repulsive core. The singularity of high potential energy at zero distance reflects the high repulsive force if the actin objects

move close enough to each other such that their electron orbitals repel strongly, but it also introduces numerical ill-conditioning.

To control this problem, we linearize the potential at distances $r \leq \epsilon$ and match potential value and slope at $r = \epsilon$, via Taylor's theorem at that point:

$$\hat{U}(x_1, x_2) = \hat{U}(r) \approx \hat{U}_\epsilon(r) \equiv \hat{U}(\epsilon) + \hat{U}'(\epsilon) \times (\|x_1 - x_2\|_2 - \epsilon), \tag{30}$$

The resulting potential function $\tilde{U}_\epsilon(r)$ is defined piecewise as the original unclipped potential for inter-molecular distance above a threshold ϵ; below that distance it becomes a linear function without discontinuity that meets the y-intercept:

$$\tilde{U}_\epsilon(r) = \begin{cases} \hat{U}(r) & r \geq \epsilon \\ \hat{U}_\epsilon(\epsilon) = \hat{U}(\epsilon) + \frac{\partial \hat{U}(r)}{\partial r}\Big|_{r=\epsilon}(r - \epsilon) & 0 \leq r \leq \epsilon \end{cases} \tag{31}$$

and therefore we have the equation below for the clipped gradient proportional to the full, clipped force:

$$\frac{\partial \tilde{U}}{\partial r}(r|\epsilon) = \begin{cases} \frac{\partial \hat{U}}{\partial r}(r) & r \geq \epsilon \\ \frac{\partial \hat{U}(r)}{\partial r}\Big|_{r=\epsilon} & 0 \leq r \leq \epsilon \end{cases} \tag{32}$$

where $r = \|x_1 - x_2\|_2$. The force is a well-defined and continuous derivative of the potential which acts to preserve Newton's laws of motion.

If G is the graph of connected filament segments, with number of nodes $|G|$ and symmetric adjacency matrix $[G_{ij} \in 0, 1]$, then the associated global energy is

$$U_{\text{radial}} = \sum_{i=1}^{|G|} \sum_{j<i} G_{ij} U_{\text{sep}}(x_i, x_j). \tag{33}$$

If we were to ignore branch points in the actin filament network, the sum of radial separation energies would decompose over filaments indexed by F and having size $|F|$:

$$U_{\text{radial}} = \sum_F \sum_{j=1}^{|F|-1} U_{\text{sep}}(x_j, x_{j+1}) \tag{34}$$

Returning to the general graph case, we calculate the gradient:

$$\begin{aligned}
\nabla_{x_l} U_{\text{radial}} &= \frac{1}{2}\sum_{i=1}^{|G|}\sum_{j\neq i} G_{ij}\nabla_{x_l} U_{\text{sep}}(x_i, x_j) \\
&= \frac{1}{2}\sum_{i=1}^{|G|}\sum_{j\neq i} G_{ij}U'_{\text{sep}}(x_i, x_j)\nabla_{x_l}\|x_i - x_j\|_2 \\
&= \frac{1}{2}\sum_{i=1}^{|G|}\sum_{j\neq i} G_{ij}U'_{\text{sep}}(x_i, x_j)\|x_i - x_j\|_2^{-1}(x_i - x_j)\cdot\nabla_{x_l}(x_i - x_j) \\
&= \frac{1}{2}\sum_{i=1}^{|G|}\sum_{j\neq i} G_{ij}U'_{\text{sep}}(x_i, x_j)\|x_i - x_j\|_2^{-1}(x_i - x_j)\cdot I(\delta_{li} - \delta_{lj}) \\
&= \frac{1}{2}\sum_{j\neq l} G_{lj}U'_{\text{sep}}(x_l, x_j)\|x_l - x_j\|_2^{-1}(x_l - x_j) - \frac{1}{2}\sum_{i\neq l} G_{il}U'_{\text{sep}}(x_i, x_l)\|x_i - x_l\|_2^{-1}(x_i - x_l)
\end{aligned} \tag{35}$$

where $\delta_{li} = 1$ if $l = i$ and 0 otherwise is the Kronecker delta function, so by symmetry, antisymmetry, and then change of index name, followed by collecting terms:

$$\begin{aligned}
\nabla_{x_l} U_{\text{radial}} &= \frac{1}{2}\sum_{j\neq l} G_{lj}U'_{\text{sep}}(x_l, x_j)\|x_l - x_j\|_2^{-1}(x_l - x_j) - \frac{1}{2}\sum_{i\neq l} G_{li}U'_{\text{sep}}(x_l, x_i)\|x_l - x_i\|_2^{-1}(x_i - x_l) \\
&= \frac{1}{2}\sum_{j\neq l} G_{lj}U'_{\text{sep}}(x_l, x_j)\|x_l - x_j\|_2^{-1}(x_l - x_j) + \frac{1}{2}\sum_{i\neq l} G_{li}U'_{\text{sep}}(x_l, x_i)\|x_l - x_i\|_2^{-1}(x_l - x_i) \\
&= \frac{1}{2}\sum_{j\neq l} G_{lj}U'_{\text{sep}}(x_l, x_j)\|x_l - x_j\|_2^{-1}(x_l - x_j) + \frac{1}{2}\sum_{j\neq l} G_{lj}U'_{\text{sep}}(x_l, x_j)\|x_l - x_j\|_2^{-1}(x_l - x_j) \\
&= \Big[\sum_{j\neq l} G_{lj}U'_{\text{sep}}(x_l, x_j)\|x_l - x_j\|_2^{-1}\Big]x_l - \Big[\sum_{j\neq l} G_{lj}U'_{\text{sep}}(x_l, x_j)\|x_l - x_j\|_2^{-1}x_j\Big].
\end{aligned} \tag{36}$$

Let

$$\psi(r) = U'_{\text{sep}}(r)/r. \tag{37}$$

Then finally

$$\nabla_{x_l} U_{\text{radial}} = \Big[\sum_{j\neq l} G_{lj}\psi(\|x_l - x_j\|)\Big]x_l - \Big[\sum_{j\neq l} G_{lj}\psi(\|x_l - x_j\|)x_j\Big]. \tag{38}$$

This is the equation we follow in the local DGG update rules below.

One consequence of Eq. (38) is

$$\frac{d\mathbf{p}}{dt} = \sum_l \mathbf{F}_l = -\sum_l \nabla_{x_l} U_{\text{radial}} = (1-1)\Big[\sum_l\sum_{j\neq l} G_{lj}\psi(x_l - x_j)x_l\Big] = 0, \tag{39}$$

conservation of the total system momentum vector.

In particular for an unbranched filament F of nonzero length $|F|$, Eq. (38) specializes to

$$\begin{aligned}\nabla_{x_{Fl}} U_{\text{radial}} = (1-\delta_{l1})(1-\delta_{l|F|})\Big(&\big(\psi(\|x_l - x_{l+1}\|_2) + \psi(\|x_{l-1} - x_l\|_2)\big)x_l \\ &- \psi(\|x_l - x_{l+1}\|_2)x_{l+1} - \psi(\|x_{l-1} - x_l\|_2)x_{l-1}\Big) \\ &+ \delta_{l1}\psi(\|x_1 - x_2\|_2)(x_1 - x_2) + \delta_{l|F|}\psi(\|x_{|F|} - x_{|F|-1}\|_2)(x_{|F|} - x_{|F|-1}).\end{aligned} \tag{40}$$

The summands in the sum in Eq. (40) correspond to separate grammar rule diagrams centered on updating node l which is an interior node connected to two other nodes of any type (first term, with $(1-\delta_{l1})(1-\delta_{l|F|})$ factor), vs. an end node at the first- or last-indexed end (second and third terms respectively, with factors of δ_{l1} and $\delta_{l|F|}$ respectively) connected to one other node of any type.

Thus for an unbranched interior filament node:

$$\begin{aligned}\nabla_{x_{Fl}} U_{\text{radial}} = &\big(\psi(\|x_l - x_{l+1}\|_2) + \psi(\|x_{l-1} - x_l\|_2)\big)x_l \\ &- \psi(\|x_l - x_{l+1}\|_2)x_{l+1} - \psi(\|x_{l-1} - x_l\|_2)x_{l-1}.\end{aligned} \tag{41}$$

The desired cancellation of longitudinal gradients along a nearly straight fiber will occur if $x_l \approx$ the weighted average of x_{l+1} and x_{l-1}, i.e. if the segment centroids are roughly colinear and equally spaced.

Under tension, the quantity ψ tends to be positive so any deviation from colinearity will generate a restoring force $\propto -\nabla U_{\text{radial}}$ bringing the middle node x_l back into line transversally, as well as towards equal longitudinal spacing. Under compression, ψ tends to be negative so transverse buckling will result.

To model random thermal displacements, it will also be necessary to calculate the Hessian matrix ∇^2_{Flm} of second derivatives. If $G_{lm} = 0$ then the Hessian matrix element is zero, so the Hessian is a weighted version of the connection graph but with self-edges added. From Eq. (38) we calculate:

$$
\begin{aligned}
\nabla^2_{x_l x_m} U_{\text{radial}} &= \delta_{lm} \sum_{j \neq l} G_{lj} \psi(\|x_l - x_j\|_2) - (1 - \delta_{lm}) G_{lm} \psi(\|x_l - x_m\|_2) \\
&+ \quad \sum_{j \neq l} G_{lj} \psi'(\|x_l - x_j\|_2) \|x_l - x_j\|_2^{-1} (x_l - x_j) \cdot I(\delta_{ml} - \delta_{mj}) \cdot (x_l - x_j) \\
&= \delta_{lm} \sum_{j \neq l} G_{lj} \psi(\|x_l - x_j\|_2) - (1 - \delta_{lm}) G_{lm} \psi(\|x_l - x_m\|_2) \\
&+ \quad \sum_{j \neq l} G_{lj} \psi'(\|x_l - x_j\|_2) \|x_l - x_j\|_2 (\delta_{ml} - \delta_{mj}) \\
&= \delta_{lm} \sum_{j \neq l} G_{lj} \Big(\psi(\|x_l - x_j\|_2) + \psi'(\|x_l - x_j\|_2)(\|x_l - x_j\|_2) \Big) \\
&\qquad - (1 - \delta_{lm}) G_{lm} \Big(\psi(\|x_l - x_m\|_2) + \psi'(\|x_l - x_m\|_2)(\|x_l - x_m\|_2) \Big)
\end{aligned} \tag{42}
$$

and finally

$$
\nabla^2_{x_l x_m} U_{\text{radial}} = \delta_{lm} \sum_{j \neq l} G_{lj} U''_{\text{sep}}(\|x_l - x_j\|_2) - (1 - \delta_{lm}) G_{lm} U''_{\text{sep}}(\|x_l - x_m\|_2). \tag{43}
$$

This is a weighted graph Laplacian. If all U'' are positive then this matrix is diagonally dominant with real eigenvalues that are all, by Gershgorin's theorem, nonnegative.

For a model of small random displacements consistent with a Boltzmann distribution with second-order (only, leaving first order effects to the gradient rules) approximation of energies, we update x_l with the Gaussian.

$$
\Pr(x'_l | x_l) \propto \exp\Big[- (x'_l - x_l)^T \Big(\Big| \sum_{j \neq l} G_{lj} U''_{\text{sep}}(\|x_l - x_j\|_2) \Big| I + \epsilon^2_{\text{sep}} I \Big) (x'_l - x_l) \Big] \tag{44}
$$

For first-order gradient dynamics we assume that, after a very brief transient ballistic behavior, our molecular-scale objects all come to force balance $F + F_{\text{drag}} = 0$ with a drag force $F_{\text{drag}} = -\zeta v$, where v is object velocity and ζ is the friction constant estimated in [13] and [18] by fitting the synaptic spine head model to experimental measurements in [32].

Thus

$$
\frac{dx_i}{dt} = \frac{F_i}{\zeta} = -\frac{1}{\zeta} \nabla_i x_i \ . \tag{45}
$$

Eq. (45) can be a stiff ODE system for inter-molecular potentials, particularly in the highly repulsive regime of the LJ potential. Thus, we introduced the clipped potential to formulate force balance (Eq. (45)) while relieving the numerical instability.

This rule in DGG implementation form is shown below.

Interior Case Anisotropic Buckling:

$$\begin{aligned} &(\bigstar_1 \longrightarrow \{\bigcirc,\square\}_2 \longrightarrow \bigstar_3) \quad \langle\!\langle\, \boldsymbol{x}_1, \boldsymbol{x}_2, \boldsymbol{x}_3 \,\rangle\!\rangle \\ \longrightarrow\ &(\bigstar_1 \longrightarrow \boxed{\{\bigcirc,\square\}_2} \longrightarrow \bigstar_3) \quad \langle\!\langle\, \boldsymbol{x}_1, \boldsymbol{x}_2, \boldsymbol{x}_3 \,\rangle\!\rangle \end{aligned} \tag{46}$$

$$\textbf{with} \quad k_{\text{kinetic}} \quad \begin{cases} \Delta_{\text{sep}}(x_1,x_2,x_3) := -\frac{1}{\zeta k_{\text{kinetic}}}\left(\frac{\partial U_{\text{trinodal, sep}}(x_1,x_2,x_3)}{\partial x_2}\right) \\ = -\frac{1}{\zeta k_{\text{kinetic}}}\left(\frac{\partial U_{\text{radial}}([x])}{\partial x_2}\right) \\ = -\frac{1}{\zeta k_{\text{kinetic}}}\Big(\psi(\|x_2-x_1\|_2)+\psi(\|x_2-x_3\|_2)\Big)x_2 \\ \qquad -\psi(\|x_2-x_1\|_2)x_1-\psi(\|x_2-x_3\|_2)x_3\Big) \end{cases}$$

This rule effectively implements a stochastic version of a forward Euler solver for Eq. (45), approaching the ODE solution as $k_{\text{kinetic}} \to \infty$. The rules of Eqs. (46), (65) below, and (70) below have in common that aside from the parameter values their LHS and RHS graphs are the same, and that only the parameters of the central node change, in a way that is computed systematically from the global biophysical energy function. For such rules we introduce the shorthand diagrammatic notation:

$$\bigcirc_1 \text{ — } \boxed{\bigcirc_2} \text{ — } \bigcirc_3 \tag{47}$$

where the boxing of node 2 is not part of the graph but serves to indicate which node has changing parameter values.

Note that the empty/filled distinction is just a visualization for a binary parameter in the actual rule objects that specifies whether the given fiber segment is an end segment, i.e. has an empty binding site for continued polymerization, or not. k_{kinetic} is a relative rate of updating biophysical (kinetic) rules; as it tends to infinity, there are more and more updates of smaller and smaller step sizes each per unit time, and the limit is an ordinary differential equation system.

Likewise, there is a special buckling rule for a filament branch point. It is mutually exclusive in domain of applicability with the interior case above, due to the constraints on actin segment objects in position 2. Defining similarly to Eq. (29)

$$U_{\text{quad-nodal,sep}}(x_1,x_2,x_3,x_4) = \tilde{U}_{\text{sep}}(x_1,x_2) + \tilde{U}_{\text{sep}}(x_2,x_3) + +\tilde{U}_{\text{sep}}(x_2,x_4)\,, \tag{48}$$

the rule is:

Branch Case Anisotropic Buckling:

$$\begin{array}{ll} \begin{pmatrix} \mathbb{O}_1 \longrightarrow \triangle_2 \longrightarrow \mathbb{O}_3 \\ \qquad\qquad\quad \searrow \\ \qquad\qquad\quad \boxdot_4 \end{pmatrix} & \langle\!\langle\ \boldsymbol{x}_1, \boldsymbol{x}_2, \boldsymbol{x}_3, \boldsymbol{x}_4\ \rangle\!\rangle \\ \longrightarrow \begin{pmatrix} \mathbb{O}_1 \longrightarrow \triangle_2 \longrightarrow \mathbb{O}_3 \\ \qquad\qquad\quad \searrow \\ \qquad\qquad\quad \boxdot_4 \end{pmatrix} & \langle\!\langle\ \boldsymbol{x}_1, \boldsymbol{x}_2 + \Delta_{\text{sep}}(x_1, x_2, x_3, x_4), \boldsymbol{x}_3, \boldsymbol{x}_4\ \rangle\!\rangle \end{array} \tag{49}$$

with k_{kinetic}

$$\begin{cases} \Delta_{\text{sep}}(x_1, x_2, x_3, x_4) := -\frac{1}{\zeta_{\text{actin}} k_{\text{kinetic}}} \left(\frac{\partial U_{\text{quad-nodal, sep}}(x_1, x_2, x_3, x_4)}{\partial x_2} \right) \\ = -\frac{1}{\zeta_{\text{actin}} k_{\text{kinetic}}} \left(\frac{\partial U_{\text{radial}}([x])}{\partial x_2} \right) \\ = -\frac{1}{\zeta_{\text{actin}} k_{\text{kinetic}}} \Big(\psi(\|x_2 - x_1\|_2) + \psi(\|x_2 - x_3\|_2) + \psi(\|x_2 - x_4\|_2) \Big) x_2 \\ \quad -\psi(\|x_2 - x_1\|_2) x_1 - \psi(\|x_2 - x_3\|_2) x_3 - \psi(\|x_2 - x_4\|_2) x_4 \Big) \end{cases}$$

The last mutually exclusive case occurs at any filament end segment. That rule is shown in Eq. (72) in Section 3.7 on filament boundary conditions.

Edges are constructed by IDs as parameters associated to objects. The forward ID is represented by the arrow, which can emanate from any object including two arrows out of a junction object to point towards an Arp2/3 object (square) as well.

Another module we add that accounts for more microscopic phenomena than the larger-scale whole ionic interactions between actin monomers is an angle bending energy that accounts for potential alignments of multiple electrostatic interaction residues between the amino acids of actin monomers. This structure imposes a constraint that the actin monomers follow the optimal bending angle created by multiple binding residues between two adjacent proteins. If the positions of three adjacent actin objects are defined as x_1, x_2, and x_3, then the angle bending potential energy is

$$U_{\text{tri-nodal, ang}}(x_1, x_2, x_3, \theta_{\text{target}}) = \frac{k_{\text{B}}}{2} \left(\cos^{-1} \left(\frac{(x_2 - x_1) \cdot (x_3 - x_2)}{\|x_2 - x_1\|_2 \|x_3 - x_2\|_2} \right) - \theta_{\text{target}} \right)^2 . \tag{50}$$

We define the scalar quantities

$$\begin{aligned} a(x_1, x_2, x_3) &= \frac{(x_2 - x_1) \cdot (x_3 - x_2)}{\|x_2 - x_1\|_2 \|x_3 - x_2\|_2} \\ b(x_1, x_2, x_3) &= \frac{\|x_3 - x_2\|_2}{\|x_2 - x_1\|_2} \\ c(x_1, x_2, x_3) &= \|x_2 - x_1\|_2 \|x_3 - x_2\|_2 \end{aligned} \tag{51}$$

Note that a is symmetric ($a(x_1, x_2, x_3) = a(x_1, x_2, x_3)$), as is c, but b isn't. Parameter $a = \cos(\theta) \in [-1, 1]$. For three colinear points with x_2 in the middle, the actual enclosed

angle $\theta = 0$ and $a = 1$. We define the vector quantities

$$\begin{aligned} L(x_1, x_2, x_3) &= (x_1 - 2x_1 + x_3) \\ \tilde{L}(x_1, x_2, x_3) &= (bx_1 - (b + \frac{1}{b})x_2 + \frac{1}{b}x_3). \end{aligned} \tag{52}$$

L is symmetric but $\tilde{L}$ is not. Then we may calculate the gradient of an interior node of three as

$$\nabla_{x_2} U_{\text{trinodal, ang}} = -k_{\text{B}} \frac{(\cos^{-1}(a) - \theta_{\text{target}})}{c\sqrt{1-a^2}} (L + a\tilde{L}) \tag{53}$$

and the gradient of an end node of three is

$$\nabla_{x_1} U_{\text{trinodal, ang}} = -k_{\text{B}} \frac{(\cos^{-1}(a) - \theta_{\text{target}})}{c\sqrt{1-a^2}} ((x_2 - x_3) - ab(x_1 - x_2)). \tag{54}$$

Our target angles are $\theta_{\text{target}} = 0$ and 70 degrees. Angles $\theta = \cos^{-1}(a)$ near 70 degrees are not a problem in the denominator but those near zero look like they might be since then $a \simeq 1$. However, for $\theta_{\text{target}} = 0$ and $a \simeq 1$ the ratio of terms is actually nonsingular by l'Hopital's rule.

The corresponding interior-node Hessian as

$$\begin{aligned} \nabla^2_{x_2 x_2} U_{\text{trinodal, ang}} &= H_{\text{interior}} + (\cos^{-1}(a) - \theta_{\text{target}}) \hat{H}_{\text{interior}} \\ H_{\text{interior}} &= \frac{k_{\text{B}}}{c^2(1-a^2)} (L + a\tilde{L}) \otimes (L + a\tilde{L}) \end{aligned} \tag{55}$$

The $(\cos^{-1}(a) - \theta_{\text{target}})\hat{H}$ term has a variable sign depending on the first factor. We will drop all such matrix terms in order to obtain a tractable, positive semidefinite approximation for use in a Gaussian distribution of position parameters for each modeled object. The resulting matrix has one nonnegative eigenvalue and (in 2D) one zero eigenvalue. We will further regularize the H matrix to make it positive definite, by taking H to be the positive eigenvalue of H_{interior} times the identity matrix, or equivalently (for a rank-one matrix) the Frobenius norm or the nuclear norm of H_{interior} times the identity matrix.

The full angle-bending potential energy is

$$U_{\text{ang}}(x, \theta_{\text{target } ijk}) = \frac{k_{\text{B}}}{2} \sum_i \sum_{j \neq i} \sum_{k \neq j,i} G_{ij} G_{jk} U_{\text{tri-nodal, ang}}(x_i, x_j, x_k, \theta_{\text{target } ijk}) \tag{56}$$

where now G^2 can be symmetrized, since any antisymmetric component will sum to zero.

We can take its gradient as

$$\nabla_l U_{\text{ang}}(x, \theta_{\text{target } ijk}) = \frac{k_{\text{B}}}{2} \sum_i \sum_{j \neq i} \sum_{k \neq j,i} G_{ij} G_{jk} \nabla_l U_{\text{tri } ijk}(x_i, x_j, x_k, \theta_{\text{target } ijk}) \tag{57}$$

$$
\begin{aligned}
\nabla_l U_{\text{ang}}(x, \theta_{\text{target } ijk}) &= -\frac{k_{\text{B}}}{2} \sum_{\langle ijk \rangle_*} G_{ij} G_{jk} \Big(\nabla_l U_{\text{tri } ilk} \delta_{jl} + \nabla_l U_{\text{tri } ljk} \delta_{il} + \nabla_l U_{\text{tri } ijl} \delta_{kl} \Big) \\
&= \frac{k_{\text{B}}}{2} \sum_{\langle ijk \rangle_*} G_{ij} G_{jk} \frac{(\cos^{-1}(a_{ijk}) - \theta_{ijk} a)}{c_{ijk} \sqrt{1 - a_{ijk}^2}} \Big[\delta_{jl} (L_{ijk} + a_{ijk} \tilde{L}_{ijk}) \\
&\quad + \delta_{il} ((x_j - x_k) - a_{ijk} b_{ijk} (x_i - x_j)) + \delta_{kl} ((x_j - x_i) - a_{kji} b_{kji} (x_k - x_j)) \Big]
\end{aligned} \tag{58}
$$

Defining

$$
\begin{aligned}
K_{ijk} &= (x_j - x_k) - a_{ijk} b_{ijk} (x_i - x_j) \\
\tilde{K}_{ijk} &= (x_j - x_i) - \frac{a_{ijk}}{b_{ijk}} (x_k - x_j) = K_{kji}
\end{aligned} \tag{59}
$$

we have

$$
\begin{aligned}
\nabla_l U_{\text{ang}}(x, \theta_{\text{target } ijk}) = &- \frac{k_{\text{B}}}{2} \sum_{\langle ijk \rangle_*} G_{ij} G_{jk} \frac{(\cos^{-1}(a_{ijk}) - \theta_{ijk})}{c_{ijk} \sqrt{1 - a_{ijk}^2}} \\
&\times \Big[\delta_{il} K_{ijk} + \delta_{kl} K_{kji} - \delta_{jl} (K_{ijk} + K_{kji}) \Big].
\end{aligned} \tag{60}
$$

K_{ijk} is not symmetric under $(i, j, k) \leftrightarrow (k, j, i)$, but of course $(K_{ijk} + K_{kji})$ is. Likewise for the "usable" portion of the Hessian,

$$
\begin{aligned}
\nabla^2_{lm} U_{\text{ang}}(x, \theta_{\text{target } ijk}) = &\frac{k_{\text{B}}}{2} \sum_{\langle ijk \rangle_*} G_{ij} G_{jk} \frac{1}{c_{ijk}^2 (1 - a_{ijk}^2)} \\
&\times \Big[\delta_{il} K_{ijk} + \delta_{kl} K_{kji} - \delta_{jl} (K_{ijk} + K_{kji}) \Big] \\
&\times \Big[\delta_{im} K_{ijk} + \delta_{km} K_{kji} - \delta_{jm} (K_{ijk} + K_{kji}) \Big] \\
&+ O(\cos^{-1}(a_{ijk}) - \theta_{\text{target } ijk}).
\end{aligned} \tag{61}
$$

Note that again the sum over l of this expression is zero, because the sum over l removes the Kronecker deltas from inside the first square bracket factor, leaving $K_{ijk} + K_{kji} - (K_{ijk} + K_{kji}) = 0$. In the l, m space this expression is a nonnegatively weighted sum of outer products of the vectors in square brackets, so the matrix is positive semidefinite.

For efficiency in implementation we need to eliminate the Kronecker deltas. So,

$$\begin{aligned}\nabla_l U_{\text{ang}}(x, \theta_{\text{target } ijk}) = -\frac{k_{\text{B}}}{2}\Bigg[& \sum_{\langle jk\rangle_{\neq};\, j,k\neq l} G_{lj}G_{jk}\frac{(\cos^{-1}(a_{ljk}) - \theta_{ljk})}{c_{ljk}\sqrt{1-a_{ljk}^2}}K_{ljk} \\ & + \sum_{\langle ij\rangle_{\neq};\, i,j\neq l} G_{ij}G_{jl}\frac{(\cos^{-1}(a_{ijl}) - \theta_{ijl})}{c_{ijl}\sqrt{1-a_{ijl}^2}}K_{lji} \\ & - \sum_{\langle ik\rangle_{\neq};\, i,k\neq l} G_{il}G_{lk}\frac{(\cos^{-1}(a_{ilk}) - \theta_{ilk})}{c_{ilk}\sqrt{1-a_{ilk}^2}}(K_{ilk} + K_{kli})\Bigg].\end{aligned} \tag{62}$$

Using relationships such as $\delta_{il}\delta_{im} = \delta_{lm}\delta_{il}\delta_{im}$ and, within the $\langle ijk\rangle_{\neq}$ sums, $\delta_{il}\delta_{km} = (1-\delta_{lm})\delta_{il}\delta_{km}$, we find a similarly reduced Hessian expression which however is the sum of nine terms rather than three. Of these nine terms, three share a factor of δ_{lm} i.e. appear on the diagonal of the Hessian, and six share a factor of $(1-\delta_{lm})$ and are therefore off-diagonal terms. For example the diagonal terms can be calculated easily:

$$\begin{aligned}\nabla^2_{lm} U_{\text{ang}}(x, \theta_{\text{target } ijk}) = \frac{k_{\text{B}}}{2}\delta_{lm}\Bigg[& \sum_{\langle jk\rangle_{\neq};\, j,k\neq l} G_{lj}G_{jk}\frac{1}{c_{ljk}^2(1-a_{ljk}^2)}K_{ljk}^2 \\ & + \sum_{\langle ij\rangle_{\neq};\, i,j\neq l} G_{ij}G_{jl}\frac{1}{c_{ijl}^2(1-a_{ijl}^2)}K_{lji}^2 \\ & + \sum_{\langle ik\rangle_{\neq};\, i,k\neq l} G_{il}G_{lk}\frac{1}{c_{ilk}^2(1-a_{ilk}^2)}(K_{ilk} + K_{kli})^2\Bigg] \\ & + (1-\delta_{lm})\Big[\ldots\Big] + O(\cos^{-1}(a_{ijk}) - \theta_{\text{target } ijk}).\end{aligned} \tag{63}$$

The terms diagonal in the l, m space suffice to define a joint Gaussian model with properly nonnegative eigenvalues, but more importantly for our purpose, to define a single-l at a time Gaussian update formula similar to Eq. (44).

$$\Pr(x_l'|x_l) \propto \exp\Big[-(x_l' - x_l)^T\Big(\Big(\sum_{\langle jk\rangle_{\neq}} G_{lj}G_{jk}\ldots + \ldots + \ldots\Big)I + \epsilon_{\text{ang}}^2 I\Big)(x_l' - x_l)\Big] \tag{64}$$

The resulting DGG update rules are:

Angle Bending 1:

$$\begin{aligned}&(\bigstar_1 \longrightarrow \bigstar_2 \longrightarrow \bigstar_3) && \langle\!\langle\, \boldsymbol{x}_1, \boldsymbol{x}_2, \boldsymbol{x}_3 \,\rangle\!\rangle \\ \longrightarrow\ &(\bigstar_1 \longrightarrow \boxed{\bigstar_2} \longrightarrow \bigstar_3) && \langle\!\langle\, \boldsymbol{x}_1, \boldsymbol{x}_2 + \Delta_{\text{ang}}(x_1, x_2, x_3), \boldsymbol{x}_3 \,\rangle\!\rangle\end{aligned} \tag{65}$$

with k_{kinetic}

$$\begin{cases}\Delta_{\text{ang}}(x_1, x_2, x_3) & := -\frac{1}{\zeta_{\text{actin}}k_{\text{kinetic}}}\frac{\partial U_{\text{tri-nodal,ang}}(x_1, x_2, x_3, \theta(\tau_1, \tau_2, \tau_3))}{\partial x_2} \\ & = -\frac{k_{\text{B}}}{\zeta_{\text{actin}}k_{\text{kinetic}}}\frac{(\cos^{-1}(a_{123}) - \theta(\tau_1, \tau_2, \tau_3))}{c_{123}\sqrt{1-a_{123}^2}}(K_{123} + K_{321})\end{cases}$$

Angle Bending 2:

$$
\begin{aligned}
&(\bigstar_1 \longrightarrow \bigstar_2 \longrightarrow \bigstar_3) && \langle\!\langle\, \boldsymbol{x}_1, \boldsymbol{x}_2, \boldsymbol{x}_3 \,\rangle\!\rangle \\
\longrightarrow &(\boxed{\bigstar_1} \longrightarrow \bigstar_2 \longrightarrow \bigstar_3) && \langle\!\langle\, \boldsymbol{x}_1 + \Delta_{\text{ang}}(x_1, x_2, x_3), \boldsymbol{x}_2, \boldsymbol{x}_3 \,\rangle\!\rangle
\end{aligned}
\tag{66}
$$

$$
\textbf{with} \quad k_{\text{kinetic}}
\begin{cases}
\Delta_{\text{ang}}(x_1, x_2, x_3) & := -\frac{1}{\zeta_{\text{actin}} k_{\text{kinetic}}} \frac{\partial U_{\text{tri-nodal,ang}}(x_1, x_2, x_3, \theta(\tau_1, \tau_2, \tau_3))}{\partial x_1} \\
& = -\frac{k_{\text{B}}}{\zeta_{\text{actin}} k_{\text{kinetic}}} \frac{(\cos^{-1}(a_{123}) - \theta(\tau_1, \tau_2, \tau_3))}{c_{123}\sqrt{1 - a_{123}^2}} K_{321}
\end{cases}
$$

... and likewise a third rule (with the directed edges reversed) for x_3. Note that the second angle-bending rule is not exclusive to filament end cases, though the first angle-bending rule will not apply to those cases. Here $\theta(\tau_1, \tau_2, \tau_3) = \theta(\tau_3, \tau_2, \tau_1)$ is the preferred (minimal-energy) angle for three successive nodes as a function of their type data (including end-node status) τ, which we have visualized with different icons ○, ● etc..

The other module we add for biophysics is aimed at providing some thermal noise for spatial fluctuations near-equilibrium which describes continual movement of the actin filaments within the context of minimizing the Hessian of the chosen potential.

Hessian Boltzmann sampling is derived from the Taylor expansion of a potential

$$
U(x + u) \approx U(x) + U'(x)^T \cdot u + \frac{1}{2} u^T \cdot H|_x \cdot u + ..., \tag{67}
$$

where x is the current state, u is a displacement vector in the state, and $H = \nabla^2 U$ is the Hessian matrix of second derivatives of U.

We extend the "heat-bath" thermal simulation algorithm to a Metropolis-Hastings version by fulfilling the following Bayesian equation for detailed balance and probability flow between two states:

$$
\frac{A(x'|x)}{A(x|x')} = \frac{p(x')q(x|x')}{p(x)q(x'|x)}, \tag{68}
$$

where x' is the new state and x is the old or current state, which we henceforth equate with position. q is the probability distribution for proposing a change from the old state to the new state. p is known as the target steady-state distribution to which we want the Markov Chain Monte Carlo (MCMC) algorithm to converge. For the Metropolis-Hastings algorithm the displacement proposal distributions are not homogeneous, and we analogously extend the "heat-bath" algorithm to a novel thermal noise algorithm that assigns displacement update probabilities according to the current state. The covariance of this multivariate Gaussian is the inverse of the Hessian multiplied by thermodynamic $k_{\text{Boltzmann}} T$ ([60]). We let the mean of the sampling distribution be zero. The linear term of the Taylor expansion – assumed to be near-zero – is accounted for instead in the viscous gradient dynamics.

In this algorithm we derive a heat-bath acceptance probability for thermal noise by considering respective forward and reverse versions of the target state probabilities $p(x)$ and proposal probabilities $q(x'|x)$, and imposing the standard constraint of

detailed balance. We consider the Boltzmann probabilities of the thermal state of a system to rely on the pure separation potential at that state. For proposal probabilities conditioned on the current state, which is our normal distribution, we take them to be proportional to the Boltzmann probability with Hessian energy term in the Taylor expansion of the current state. When the acceptance probabilities are algebraically manipulated into heat-bath form, we find that the acceptance probability takes the form

$$A(x'|x) = \frac{e^{-\frac{\Delta U - \Delta U_q}{k_{\text{Boltzmann}} T}} \sqrt{|H(x)/H(x')|}}{1 + e^{-\frac{\Delta U - \Delta U_q}{k_{\text{Boltzmann}} T}} \sqrt{|H(x)/H(x')|}} \tag{69}$$

where U is the global mechanical energy, ΔU is the change in U due to a local move from x to x', U_q is just the quadratic (Hessian) part of the local Taylor expansion (Eq. (67)) of U, $|H(x)|$ is the determinant of the Hessian $H(x)$ at x, and $\Delta U_q(x'|x) = U_q(x'|x) - U_q(x|x')$. The constant term of course drops out under the difference Δ operation. The factors of $\sqrt{|H(x')|}$ arise from a Gaussian integral approximation to the partition function normalization $\int dx \exp(-\beta U_q(x|x'))$ for the heat bath move proposal $q(x|x')$, which depends on move starting position x'.

If we instead used both the linear and quadratic terms as in Eq. (4.7) of [61], then the approximation of ΔU would be better except near the local energy minimum, leading to good acceptance ratios A. However, we opt to separate thermal noise from active drive processes in the rule set since they are physically distinct. The two options are equivalent near the local energy minimum, at thermal equilibrium or quasi-equilibrium. The probability of a "proposal" step under ΔU_q will be a zero-mean Gaussian or Normal distribution with precision matrix (inverse covariance matrix) $H/k_{\text{Boltzmann}}T$. The acceptance of such a step will depend strongly on its alignment with the gradient where the gradient is high, but will be suitably thermal near energy minima in the manner of an Ornstein-Uhlenbeck process.

We have calculated above the relevant Hessians for both buckling and bending energies. These Hessians can be summed together or, if one is expected to be substantially smaller in a matrix norm sense than the other, only the larger one can be kept. Since the central LJ-style potentials can have high derivative values at the cores, we retain just the buckling Hessian. Then, for a change in one particular $\overrightarrow{x_i}$ alone,

$$\Delta_i U([x]) = \Delta_i U_{\text{sep}}(\overrightarrow{x_i}|\text{nbd}(x_i)),$$

i.e. only local summands of U_{sep} are involved.

The DGG rule is shown below.

Hessian Thermal Noise:

$$
\begin{aligned}
&(\bigstar_1 \longrightarrow \bigstar_2 \longrightarrow \bigstar_3) \quad \langle\!\langle\, \boldsymbol{x}_1, \boldsymbol{x}_2, \boldsymbol{x}_3 \,\rangle\!\rangle \\
\longrightarrow\ &(\bigstar_1 \longrightarrow \boxed{\bigstar_2} \longrightarrow \bigstar_3) \quad \langle\!\langle\, \boldsymbol{x}_1, \boldsymbol{x}_2 + \Delta_H, \boldsymbol{x}_3 \,\rangle\!\rangle
\end{aligned}
\tag{70}
$$

$$
\textbf{with} \quad k_{\text{kinetic}} p(\Delta U_H(x_1, x_2, x_3)) \mathcal{N}(\Delta_H; 0, \Sigma_{\text{therm}})
$$

$$
\begin{cases}
p(\Delta U_H(x_1, x_2, x_3)) := \dfrac{e^{-\frac{\Delta U(x_1,x_2,x_3) - \Delta U_q(x_1,x_2,x_3)}{k_{\text{Boltzmann}} T}}}{1 + e^{-\frac{\Delta U(x_1,x_2,x_3) - \Delta U_q(x_1,x_2,x_3)}{k_{\text{Boltzmann}} T}}} \sqrt{|H(x_2)/H(x_2 + \Delta_H)|} \\
\Sigma_{\text{therm}} := 2 \frac{k_{\text{Boltzmann}} T}{\zeta_{\text{actin}} k_{\text{kinetic}}} H^{-1}(x_2)
\end{cases}
$$

For consistency we also need to include the actin fiber end case. It is in section 3.7 below.

Next, we explain how the dynamics of the membrane can be implemented in the DGG simulation also in the form of stochastic rules. There are three terms which comprise the total membrane energy: membrane area energy, membrane length energy, and membrane Helfrich mean curvature energy for the spine head membrane ([18]). The total energy is

$$
U_{\text{mem}} = 2\kappa \int_{\Gamma} (H^2) d\bar{w}. \tag{71}
$$

Here, κ the bending modulus, Γ the 1D representation of the manifold that is the 2D spine head membrane surface, H the mean curvature, and $\bar{w}$ the arc length ([19]). Mean curvature is approximated using forward finite differences.

Parameters used in our simulations are provided in Table 1.

3.6 Efficient implementation

We have approached the issue of computational efficiency in our simulation in multiple ways including rule-writing, and biophysical theory.

In rule-writing, we sample tri-nodal forces so that the net update is weaker in magnitude than pairwise forces, and anisotropic towards a perpendicular axis. In theory of biophysical kinetics, we derived a clipping potential (Eq. (31)) that sets the force to a constant value past a multiplicative factor below the optimal length. Also, the bending energy's gradient and Hessian are simplified to a few terms (Eqs. (62) and (63)).

For the filament breaking rule (Eq. (23)), we store an angle parameter for each actin node, such that all internal angles are not re-computed at each step, but the angle of each node is updated with the firing of a stochastic spatial rule that samples it. Then, they are accessed by Eq. (23) by its "with" clause.

3.7 Boundary conditions

The first boundary condition rule is for buckling. It is mutually exclusive in domain of applicability with the previous two (interior and junction node) cases.

End Case Anistropic Buckling:

$$\begin{array}{ll} (\bigstar_1 \text{ —— } \{\bullet, \blacksquare\}_2) & \langle\!\langle\ \boldsymbol{x}_1, \boldsymbol{x}_2\ \rangle\!\rangle \\ \longrightarrow (\bigstar_1 \text{ —— } \boxed{\{\bullet, \blacksquare\}_2}) & \langle\!\langle\ \boldsymbol{x}_1, \boldsymbol{x}_2 + \Delta_{\text{sep}}(x_1, x_2)\ \rangle\!\rangle \end{array} \tag{72}$$

$$\textbf{with} \quad k_{\text{kinetic}} \begin{cases} \Delta_{\text{sep}}(x_1, x_2) := -\frac{1}{\zeta_{\text{actin}} k_{\text{kinetic}}} \left(\frac{\partial U_{\text{sep}}(x_1, x_2)}{\partial x_2} \right) \\ = -\frac{1}{\zeta_{\text{actin}} k_{\text{kinetic}}} \left(\frac{\partial U_{\text{radial}}([x])}{\partial x_2} \right) \\ = -\frac{1}{\zeta_{\text{actin}} k_{\text{kinetic}}} \psi(\|x_2 - x_1\|_2)(x_2 - x_1) \end{cases}$$

Likewise, the Hessian Thermal Noise end case is:

End Case Hessian Thermal Noise:

$$\begin{array}{ll} (\{\bullet, \blacksquare\}_1 \text{ —— } \bigstar_2) & \langle\!\langle\ \boldsymbol{x}_1, \boldsymbol{x}_2\ \rangle\!\rangle \\ \longrightarrow (\boxed{\{\bullet, \blacksquare\}_1} \text{ —— } \bigstar_2) & \langle\!\langle\ \boldsymbol{x}_1 + \Delta_H, \boldsymbol{x}_2\ \rangle\!\rangle \end{array} \tag{73}$$

$$\textbf{with} \quad k_{\text{kinetic}} p(\Delta U_H(x_1, x_2)) \mathcal{N}(\Delta_H; 0, \Sigma_{\text{therm}}) \begin{cases} p(\Delta U_H(x_1, x_2)) := \frac{e^{-\frac{\Delta U(x_1, x_2) - \Delta U_q(x_1, x_2)}{k_{\text{Boltzmann}} T}} \sqrt{|H(x_1)/H(x_1 + \Delta_H)|}}{1 + e^{-\frac{\Delta U(x_1, x_2) - \Delta U_q(x_1, x_2)}{k_{\text{Boltzmann}} T}} \sqrt{|H(x_1)/H(x_1 + \Delta_H)|}} \\ \Sigma_{\text{therm}} := 2 \frac{k_{\text{Boltzmann}} T}{\zeta_{\text{actin}} k_{\text{kinetic}}} H^{-1}(x_2) \end{cases}$$

In each of these rules the undirected edge on both LHS and RHS is a shortand notation for a pair of directed-edge rules. In the first of the pair, both undirected edges are replaced with edges directed in the same left-to-right direction in the picture; and in the second of the pair, both undirected edges are replaced with edges directed in the same right-to-left direction.

4 Discussion

We have demonstrated how to use our Dynamical Graph Grammar (DGG) simulation to reveal trends of actin cytoskeletal elements on dendritic spine head membrane expansion in 2D. The results support the existence of biophysical effects from the number of ABPs bound to actin filament networks. In particular CaMKIIβ molecules are affected by Arp2/3 and are hypostatic in growth of spine head during the growth phase of a model for long-term potentiation. Cofilin, in large numbers, counteracts Arp2/3 based growth. There can be net effects from combined mechanisms, e.g. mechanical bending relaxation and filament breaking, as shown by cofilin's impact on membrane size. The addition of Aip1 as a filament severing molecule to the model provided greater certainty about the role of other ABPs than through cofilin as the sole severing molecule. The DGG modeling language easily accommodated model variations and elaborations pertaining to cytoskeleton in dendritic spine.

An important advancement of our model is the method of biophysics modules in a DGG modeling language. The symbolic expressiveness of our stochastic simulator allows non-linear representations for velocity gradient and thermal noise Hessian based

Parameter	Value	Description
k_{kinetic}	$0.35\ \frac{1}{\text{s}}$	Kinetics propensity
$r_{\text{spinehead, init}}$	$0.125\ \mu\text{m}$	Starting spine head radius
N_{CG}	12 monomers	Number of actin monomers in a coarse-grained object
T	310 K	Temperature
$k_{\text{Boltzmann}}$	$1.38 \times 10^{-23}\ \frac{\text{J}}{\text{K}}$	Boltzmann's constant
ϵ_{Clip}	0.75	Clipping factor for LJ potential
θ_{Arp}	70°	Arp2/3 branching angle ([62])
k_{s}	$15.9\ \frac{\text{N}}{\text{m}}$	Spring constant of adjacent actin monomers ([20])
k_{B}	$4.0 \times 10^{-26}\ \text{N}m^2$	Bending stiffness of actin filament ([63])
$k_{\text{B, Arp}}$	$k_{\text{B}}\ \text{N}m^2$	Bending stiffness of Arp2/3 branch
ϵ_{LJ}	$7.36 \times 10^{-16}\ \text{J}$	Dissociation energy for LJ potential ([64])
$\mathcal{D}_{\mathcal{U}}$	$0.0175\ \mu\text{m}$	Binding distance constraint for CaMKIIβ
θ_{Bundle}	15°	Bundling angle constraint for CaMKIIβ ([65])
$k_{\text{s, Arp2/3}}$	$20\ \frac{N}{m}$	Spring constant for branch bond to F-actin ([65])
$k_{\text{s, CaMKII}\beta}$	$20\ \frac{N}{m}$	Spring constant for bundling bond to F-actin ([65])
$k_{\text{B, CaMKII}\beta}$	$k_{\text{s, Cam}}$	Bending stiffness for CaMKIIβ bundling segment
ζ_{actin}	$500\ \frac{\text{N}}{\text{m/s}}$	Friction coefficient of actin network ([18])
ζ_{mem}	$500\ \frac{\text{N}}{\text{m/s}}$	Friction coefficient of membrane vertex([18])
L_p	$17.7 \times 10^{-6}\ \text{m}$	Persistence length of actin filament ([66])
$\theta_{\text{break, Actin}}$	57°	Breaking angle of bare actin ([59])
$\theta_{\text{break, Cofilactin}}$	73°	Breaking angle of cofilactin ([59])
$\theta_{\text{break, Boundary}}$	31°	Breaking angle of actin-cofilactin boundary ([59])
$k_{\text{barbed, on, ATP}}$	$11.6 \times 10^6\ \frac{1}{\text{M}\cdot\text{s}}$	Barbed end elongation rate constant (ATP) ([49])
$k_{\text{barbed, off, ATP}}$	$1.4\ \frac{1}{\text{s}}$	Barbed end retraction rate constant (ATP) ([49])
$k_{\text{pointed, on, ATP}}$	$1.3 \times 10^6\ \frac{1}{\text{M}\cdot\text{s}}$	Pointed end elongation rate constant (ATP) ([49])
$k_{\text{pointed, off, ATP}}$	$0.81\ \frac{1}{\text{s}}$	Pointed end retraction rate constant (ATP) ([49])
$k_{\text{barbed, on, ADP}}$	$3.8 \times 10^6\ \frac{1}{\text{M}\cdot\text{s}}$	Barbed end elongation rate constant (ADP) ([49])
$k_{\text{barbed, off, ADP}}$	$7.2\ \frac{1}{\text{s}}$	Barbed end retraction rate constant (ADP) ([49])
$k_{\text{pointed, on, ADP}}$	$0.16 \times 10^6\ \frac{1}{\text{M}\cdot\text{s}}$	Pointed end elongation rate constant (ADP) ([49])
$k_{\text{pointed, off, ADP}}$	$0.27\ \frac{1}{\text{s}}$	Pointed end retraction rate constant (ADP) ([49])
k_{branch}	$3000.\ \frac{1}{\text{M}\cdot\text{s}}$	Arp2/3 nucleation rate ([67])
k_{unbranch}	$0.47\ \frac{1}{\text{s}}$	Unbinding of Arp2/3 ([67])
$k_{\text{cap, on}}$	$6.3 \times 10^6\ \frac{1}{\text{M}\cdot\text{s}}$	Barbed end capping on rate constant ([68])
$k_{\text{cap, off}}$	$9.5 \times 10^{-4}\ \frac{1}{\text{s}}$	Aip1 end-capping off rate constant ([69])
$k_{\text{CaMKII}\beta\text{, on}}$	$0.5 \times 10^6\ \frac{1}{\text{M}\cdot\text{s}}$	Binding rate constant of CaMKIIβ ([70])
$k_{\text{CaMKII}\beta\text{, off}}$	$0.23\ \frac{1}{\text{s}}$	Unbinding rate constant of CaMKIIβ ([70])
$k_{\text{ATP, Hydrolysis}}$	$0.35\ \frac{1}{\text{s}}$	ATP hydrolysis rate constant on actin filaments ([71])
$k_{\text{cof, Pi}}$	$0.035\ \frac{1}{\text{s}}$	Release of Pi from actin filament with nearby cofilin ([71])
k_{Pi}	$0.006\ \frac{1}{\text{s}}$	Release of Pi from actin filament ([71])
$k_{\text{cof-on, edge, ADP}}$	$17 \times 10^6\ \frac{1}{\text{M}\cdot\text{s}}$	Recruitment of cofilin to bound cofilin in ADP presence ([72])
$k_{\text{cof-off}}$	$0.7\ \frac{1}{\text{s}}$	Unbinding of cofilin from actin filament ([72])
$k_{\text{single, on, Cof}}$	$10^4\ \frac{1}{\text{M}\cdot\text{s}}$	On rate constant of isolated Cof. ([55])
k_{sever}	$1.43\ \frac{1}{\text{s}}$	Rate of severing by Aip1 ([48])
$k_{\text{on, Aip1}}$	$112 \times 10^6\ \frac{1}{\text{M}\cdot\text{s}}$	On rate of Aip1 to cofilactin ([69])
k_{debranch}	2×10^{-3}	De-branching rate from parent filament ([54])
σ_{comp}	4.0	Competition constant for cofilin against Arp2/3 ([54])
$k_{\text{synth, actin}}$	$19.5 \times 10^{-6}\ \frac{\text{M}}{\text{s}}$	Basal synthesis rate of actin([13, 30, 32])
$k_{\text{influx, actin}}$	$18.8 \times 10^{-6}\ \frac{\text{M}}{\text{s}}$	Stim. synthesis rate of actin ([13, 30, 32])
$k_{\text{deg, actin}}$	$0.096\ \frac{1}{\text{s}}$	Degradation rate of actin ([13, 32])
$k_{\text{synth, arp2/3}}$	$2.6 \times 10^{-6}\ \frac{\text{M}}{\text{s}}$	Basal synthesis rate of Arp2/3 ([13, 32])
$k_{\text{influx, arp2/3}}$	$0.41 \times 10^{-6}\ \frac{\text{M}}{\text{s}}$	Stim. synthesis rate of Arp2/3 ([13, 32])
$k_{\text{deg, arp2/3}}$	$0.053\ \frac{1}{\text{s}}$	Degradation rate of Arp2/3 ([13, 32])
$k_{\text{synth, cof}}$	$0.47 \times 10^{-6}\ \frac{\text{M}}{\text{s}}$	Basal synthesis rate of cof. ([13, 32])
$k_{\text{influx, cof}}$	$0.78 \times 10^{-6}\ \frac{\text{M}}{\text{s}}$	Stim. synthesis rate of cof. ([13, 32])
$k_{\text{deg, cof}}$	$0.057\ \frac{1}{\text{s}}$	Degradation rate of cof. ([13, 32])
$k_{\text{synth, CaMKII}\beta}$	$4.29 \times 10^{-6}\ \frac{\text{M}}{\text{s}}$	Basal synthesis rate of CaMKIIβ([13, 30, 32])
$k_{\text{influx, CaMKII}\beta}$	$-1.96 \times 10^{-6}\ \frac{\text{M}}{\text{s}}$	Stim. synthesis rate of CaMKIIβ([13, 30, 32])
$k_{\text{deg, CaMKII}\beta}$	$0.052\ \frac{1}{\text{s}}$	Degradation rate of CaMKIIβ ([13, 32])
$k_{\text{synth, cap}}$	$0.0046 \times 10^{-6}\ \frac{\text{M}}{\text{s}}$	Basal synthesis rate of end-capping protein ([13, 32])
$k_{\text{influx, cap}}$	$0.0014 \times 10^{-6}\ \frac{\text{M}}{\text{s}}$	Stim. synthesis rate of end-capping protein ([13, 32])
$k_{\text{deg, cap}}$	$0.052\ \frac{1}{\text{s}}$	Degradation rate of end-capping protein ([13, 32])
κ	$0.0005\ \text{pN}\mu\text{m}$	Membrane curvature strength ([18])

Table IV: Table of parameters used in DGG simulations.

on an anharmonic potential compared to an integrator requiring linearization of the instantaneous force like Cytosim ([10]). Implementation of biophysics in a stochastic grammar simulator that is event-based rather than looping over objects is more efficient than computation of inter-object potential (Eq. (28)) gradient for every interaction, which would additionally require more calibration of time step for effective wall clock simulation run time. The DGG stochastic algorithm handles time-stepping efficiently in a way that adapts to computational burden from the increasing size of pool of objects. We can update the combinatorial casework and physical update equations in biophysical rules in a DGG grammar whereas simulators like Cytosim are a predetermined numerical integration algorithm that is difficult to update according to physical theory.

Our model can reveal epistatic relationships between cytoskeleton binding proteins. For the transient growth phase of a model of stubby spine head long-term potentiation, we find that Arp2/3 is epistatic to CaMKIIβ. Such a relationship can be used to determine which protein masks another protein's effect under control conditions of the rest of the ABPs in the model. We observe benefits of the Aip1 extension on the relation of ABPs to stubby spine head morphology. In the model without Aip1, there is greater uncertainty for the role of each of three ABPs (Arp2/3, CaMKIIβ, cofilin), and Arp2/3, the network branching protein, dominates the contribution to spine head morphology. The new model is clear in the role of each ABP included in it (sections 2.1–2.3), with a reduction in the role of Arp2/3.

Consistent with previous experimental studies discussed in Section 2.3, we find that cofilin reduces spine head size. Our modeling result shows that, under our modeling conditions, actin filament severing by Aip1 increases spine head size. A mutually exclusive implementation of competitive binding to actin filaments between cofilin and Arp2/3 as well as between cofilin and CaMKIIβ in our model is a reason for decreased spine head size from increased cofilin synthesis. We hypothesize that the competitive binding between cofilin and Arp2/3 means increased number of bound cofilin limits the extent the actin network can grow by limiting branching events. The severing events that occur under this increasingly limiting factor are also further limited by CaMKIIβ binding events to the newly polymerized locations of actin filaments, aligned in parallel by the severing events that do not depend on a breaking angle, that disallow recruitment of cofilin to neighboring unbound locations on actin filaments. The role of cofilin that does occur under inclusion of Aip1 is weakening of angular bending stiffness, which decreases the ability of filaments to push the membrane to grow in size. The role of Aip1 in severing actin filaments by binding to cofilactin has been determined by biological experiment recently ([47]), explaining previous speculation about Aip1 affecting actin filament severing rate ([48]), and we include it as a mechanistic extension in our model with the addition of just a few simpler rules to the pre-existing several hundred rules. The DGG modeling language has proven to be highly expressive in representing biological, biochemical, and biophysical knowledge in an extensible way in this domain, as we scaled up the number of rules and the amount of detail they express.

There are many avenues for future work to extend our model. Additional modules can be incorporated by design of DGGs for new cytoskeletal elements. Simulations can

reach bigger scales of the spine head receiving timed signals. Implementation in the more numerically powerful, accelerated DGGML simulation package ([27, 73, 74]), of DGG in C++, currently two-dimensional but with three dimensions under development, may enable large 3D simulations and may include model reduction assistance by AI ([12]). Usage of larger coarse-graining numbers would feasibly simulate changes to a synaptic spine head on a long-term scale. The result would be exploration of long-term potentiation using graph-based actin cytoskeletal simulation in synaptic spine heads, also of larger sizes, ultimately to understand mechanisms associated with learning and protect and enhance memory.

Molecular dynamics (MD) simulation, e.g. [75], is similar to our simulation system in that it updates positions of simulation objects, but also exhibit differences that make DGGs more suitable for spine head simulation. MD simulations are slow, simulating on at most the nanosecond or even femtosecond scale; DGGs can operate on much coarser spatial and temporal scales, and can naturally update the number or nature of chemical species or objects in the simulation. So, they work well for remodeling of the actin cytoskeleton. MD simulations use ballistic movement while we implement viscous dynamics to convert forces to velocity in coarse-scale models represented as DGGs, as is appropriate in a viscous medium and spatial scale on all but the fastest time scales. In this way, we provide an efficient, expressive, and suitable simulation for spine head dynamics.

Our graph-based simulation algorithm is able to implement the biophysical model from underlying principles. It is a highly expressive simulation system that incorporates many modules well-suited for changing both network topology and spatial or, more generally, agent-associated parameters. DGGs offer considerable advantages over modern cytoskeletal simulation software, in the ability to offer users rule-based control to implement spatial, non-spatial, and protein-based regulation of the actin cytoskeleton by ABPs based on satisfying constraints. This format is made possible due to the availability of parameterizations associated with objects in both pattern-matching and object-replacements and the convenient, declarative usage of the "with" clause in the DGG modeling language.

Four ABPs, out of many more actin regulatory ABPs, have been implemented in the simulation as a demonstration of such a system's interoperability with DGGs. They represent the major cytoskeleton remodeling mechanisms known about actin filament networks. Non-spatial rules associated with regulatory ABPs, will usually have less casework for rule implementation, as the spatial rules are tri-nodal or quad-nodal (junctions) in actin filament sub-graph matching. As a model of learning and memory, we find that simulations of the synaptic spine head not only provide insight into the molecule types of the simulation, but also allow for a new kind of artificial intelligence capability that is spatial and biophysical in a unit of learning. Moreover, as symbolic and graphical artificial intelligence systems ([76]), DGGs and their rulesets could function as intelligent counterparts of biological systems.

Inherent patterns of the system have been characterized, with several implications: (1) There may also be an advantage for model reduction of this system using artificial neural networks which have nonlinear activation functions to capture spine head

behavior. This would result in faster predictions about synaptic spine heads with biological experiments. (2) A memory protein can be a node inside an epistatic relation as demonstrated in this paper. (3) The current DGG formalism is available for simulation of long-term effects of ABPs.

Such computational observations may in the future be compared to experiment, perhaps after further modeling such as the extension of the present model to three dimensions.

Declarations

Funding

This work was funded in part by U.S. NIH/NIDA Brain Initiative Grant 1RF1DA055668-01 (all coauthors), and also by Human Frontiers Science Program Grant HFSP—RGP0023/2018 (EM), NIH NIMH CRCNS R01-MH129066 (TS, TB), NSF NeuroNex DBI-1707356 (TS, TB), and NSF NeuroNex DBI-2014862 (TS, TB). This work was supported in part by the UC Southern California Hub, with funding from the UC National Laboratories division of the University of California Office of the President (EM).

Author Contributions

TB, TS, and EM designed the research. MH implemented the kinetic rules, carried out all simulations, and analyzed the data. EM provided the DGG theory and the derivation of kinetic rules from a global energy function. TB designed the cytoskeleton structure-altering rules, with domain expertise from PR. MH, and EM wrote the paper.

Competing interests

P.R. is a consultant for Simula Research Laboratories in Oslo, Norway and receives income. The terms of this arrangement have been reviewed and approved by the University of California, San Diego in accordance with its conflict-of-interest policies. E.M. has a Joint Appointment with the Los Alamos National Laboratory Computer, Computational, and Statistical Sciences Division. The terms of this arrangement have been reviewed and approved by the University of California, Irvine, in accordance with its conflict-of-interest policies.

Acknowledgements

We thank Mayte Bonilla-Quintana for many substantial modeling discussions regarding the actin cytoskeleton in dendritic spine head. We thank Elliot Meyerowitz, Sean Wilson, and Katherine Thompson-Peer for useful discussions. We thank Arthur York for creating a previous version of the DGG model file including cytoskeleton structure-altering rules.

Ethics approval and consent to participate

Not applicable.

Consent for publication

Data availability

Not applicable.

Materials availability

The Plenum DGG modeling language package written in Mathematica by Guy Yosiphon is available at https://computableplant.ics.uci.edu/theses/guy/Plenum.html [17]. Another version of Plenum, with very small modification to run this paper's simulation code, is available at the GitHub repository https://github.com/matthewhur836/SpineHead-DGG under a sub-directory.

Code availability

The DGG modeling code for this paper, written using the Plenum DGG modeling package, is available at the GitHub repository https://github.com/matthewhur836/SpineHead-DGG.

References

[1] Hotulainen, P. & Hoogenraad, C. C. Actin in dendritic spines: connecting dynamics to function. *J Cell Biol* **189**, 619–629 (2010).

[2] Araya, R., Vogels, T. P. & Yuste, R. Activity-dependent dendritic spine neck changes are correlated with synaptic strength. *Proc Natl Acad Sci U S A* **111**, E2895–E2904 (2014).

[3] Hebb, D. O. *The Organization of Behavior* 1 edn (Psychology Press, United Kingdom, 2002).

[4] Bonilla-Quintana, M. & Rangamani, P. Can biophysical models of dendritic spines be used to explore synaptic changes associated with addiction? *Phys Biol* **19** (2022).

[5] Lisman, J. Criteria for identifying the molecular basis of the engram (CaMKII, PKMzeta). *Mol Brain* **10**, 55 (2017).

[6] Lee, C. T., Bell, M., Bonilla-Quintana, M. & Rangamani, P. Biophysical modeling of synaptic plasticity. *Annu Rev Biophys* **53**, 397–426 (2024).

[7] A, H. P., Basavaraju, N., Gupta, A. & Kommaddi, R. P. Actin cytoskeleton at the synapse: An Alzheimer's Disease perspective. *Cytoskeleton (Hoboken)* (2025).

[8] Okamoto, K.-I., Narayanan, R., Lee, S. H., Murata, K. & Hayashi, Y. The role of CaMKII as an f-actin-bundling protein crucial for maintenance of dendritic spine structure. *Proc Natl Acad Sci U S A* **104**, 6418–6423 (2007).

[9] Yasuda, R., Hayashi, Y. & Hell, J. W. CaMKII: a central molecular organizer of synaptic plasticity, learning and memory. *Nat Rev Neurosci* **23**, 666–682 (2022).

[10] Nedelec, F. & Foethke, D. Collective langevin dynamics of flexible cytoskeletal fibers. *New J Phys* **9** (2007).

[11] Abekhoukh, S. & Bardoni, B. CYFIP family proteins between autism and intellectual disability: links with Fragile X syndrome. *Front Cell Neurosci* **8** (2014).

[12] Mjolsness, E. Prospects for declarative mathematical modeling of complex biological systems. *Bull Math Biol* **81**, 3385–3420 (2019).

[13] Bonilla-Quintana, M. & Rangamani, P. Biophysical modeling of actin-mediated structural plasticity reveals mechanical adaptation in dendritic spines. *eNeuro* **11** (2024).

[14] Hernandez-Aristizabal, D., Garzon-Alvarado, D.-A., Duque-Daza, C.-A. & Madzvamuse, A. A bulk-surface mechanobiochemical modelling approach for single cell migration in two-space dimensions. *J Theor Bio* **595**, 111966 (2024).

[15] Mjolsness, E. Explicit calculation of structural commutation relations for stochastic and dynamical graph grammar rule operators in biological morphodynamics. *Front Syst Biol* **2**, 898858 (2022).

[16] Mjolsness, E. & Yosiphon, G. Stochastic process semantics for dynamical grammars. *Ann Math Artif Intell* **47**, 329–395 (2006).

[17] Yosiphon, G. *Stochastic parameterized grammars: Formalization, inference, and modeling applications.* Ph.D. thesis, University of California, Irvine (2009).

[18] Bonilla-Quintana, M., Wörgötter, F., Tetzlaff, C. & Fauff, M. Modeling the shape of synaptic spines by their actin dynamics. *Front Synaptic Neuroscience* **12** (2020).

[19] Bonilla-Quintana, M., Wörgötter, F., D'este, E., Tetzlaff, C. & Fauff, M. Reproducing asymmetrical spine shape fluctuations in a model of actin dynamics predicts self-organized criticality. *Sci Rep* **11**, 4012 (2021).

[20] Mogilner, A. & Oster, G. Force generation by actin polymerization ii: The elastic ratchet and tethered filaments. *Biophys J* **84**, 1591–1605 (2003).

[21] Ni, H. & Papoian, G. A. Simulating deformable vesicles containing complex cytoskeletal networks. *J Phys Chem B* **125**, 10710–10719 (2021).

[22] Akamatsu, M. *et al.* Principles of self-organization and load adaptation by the actin cytoskeleton during clathrin-mediated endocytosis. *eLife* e49840 (2020).

[23] Serwas, D. *et al.* Mechanistic insights into actin force generation during vesicle formation from cryo-electron tomography. *Dev Cell* **57**, 1132—-1145 (2022).

[24] Bader, J. S., Berne, B. J., Pollak, E. & Hänggi, P. The energy relaxation of a nonlinear oscillator coupled to a linear bath. *J Chem Phys* **104**, 1111—-1119 (1996).

[25] Tuckerman, M. & Berne, B. J. Vibrational relaxation in simple fluids: comparison of theory and simulation. *J Chem Phys* **98**, 7301–7318 (1993).

[26] Mjolsness, E. Quantitative symbolic process models: How a fair fraction of intelligence could be abstracted in AI research. Tech. Rep. FS-13-02, AAAI (2013).

[27] Medwedeff, E. & Mjolsness, E. Approximate simulation of cortical microtubule models using dynamical graph grammars. *Phys Biol* **11** (2023).

[28] Schünemann, K. D. *et al.* Comprehensive analysis of human dendritic spine morphology and density: Exploring diversity of human dendritic spines. *bioRxiv* (2024).

[29] Pchitskaya, E. & Bezprozvanny, I. Dendritic spines shape analysis - classification or clusterization? perspective. *Front Synaptic Neurosci* **12** (2020).

[30] Helm, M. S. *et al.* A large-scale nanoscopy and biochemistry analysis of postsynaptic dendritic spines. *Nat Neurosci* **24** (2021).

[31] Shonesy, B. C., Jalan-Sakrikar, N., Cavener, V. S. & Colbran, R. J. CaMKII: a molecular substrate for synaptic plasticity and memory. *Prog Mol Biol Transl Sci* **122**, 61–87 (2014).

[32] Bosch, M. *et al.* Structural and molecular remodeling of dendritic spine substructures during long-term potentiation. *Neuron* 444–459 (2014).

[33] Matsuzaki, M., Honkura, N., Ellis-Davies, G. C. & Kasai, H. Structural basis of long-term potentiation in single dendritic spines. *Nature* **429**, 761–766 (2004).

[34] Voronin, L. L. Long-term potentiation in the hippocampus. *Neuroscience* **10**, 1051–1069 (1983).

[35] Gentile, J. E., Carrizales, M. G. & Koleske, A. J. Control of synapse structure and function by actin and its regulators. *Cells* **11**, 603 (2022).

[36] Kim, K. *et al.* A temporary gating of actin remodeling during synaptic plasticity consists of the interplay between the kinase and structural functions of CaMKII. *Neuron* **87**, 813–26 (2015).

[37] Wang, Q. *et al.* Assemblies of calcium/calmodulin-dependent kinase ii with actin and their dynamic regulation by calmodulin in dendritic spines. *Proc Natl Acad Sci U S A* **116**, 18937–18942 (2019).

[38] Avery, L. & Wasserman, S. Ordering gene function: the interpretation of epistasis in regulatory hierarchies. *Trends Genet* **8**, 312–6 (1992).

[39] Pi, H. J. *et al.* CaMKII control of spine size and synaptic strength: Role of phosphorylation states and nonenzymatic action. *Proc Natl Acad Sci U S A* **107**, 14437–42 (2010).

[40] Asrican, B., Lisman, J. & Otmakhov, N. Synaptic strength of individual spines correlates with bound Ca2+–Calmodulin-Dependent Kinase II. *J Neurosci* **27**, 14007–14011 (2007).

[41] Zernov, N., Bezprozvanny, I. & Popugaeva, E. CaMKIIβ knockdown decreases store-operated calcium entry in hippocampal dendritic spines. *IBRO Neurosci Rep* **12**, 90–97 (2022).

[42] Paciello, F. *et al.* Role of LIMK1-cofilin-actin axis in dendritic spine dynamics in Alzheimer's disease. *Cell Death and Disease* **16** (2025).

[43] Pontrello, C. G. *et al.* Cofilin under control of β-arrestin-2 in NMDA-dependent dendritic spine plasticity, long-term depression (LTD), and learning. *Proc Natl Acad Sci U S A* **109**, E442–E451 (2012).

[44] Rust, M. B. ADF/cofilin: a crucial regulator of synapse physiology and behavior. *Cell Mol Life Sci* **72**, 3521—-3529 (2015).

[45] Calabrese, B., Saffin, J.-M. & Halpain, S. Activity-dependent dendritic spine shrinkage and growth involve downregulation of cofilin via distinct mechanisms. *PLoS One* **9**, e94787 (2014).

[46] Raven, F. *et al.* Cofilin overactivation improves hippocampus-dependent short-term memory. *Front Behav Neurosci* **17** (2023).

[47] Oosterheert, W., Sanders, M. B., Hofnagel, O., Bieling, P. & Raunser, S. Choreography of rapid actin filament disassembly by coronin, cofilin, and aip1. *Cell* **188**, 6845–6860 (2025).

[48] Chen, Q., Courtemanche, N. & Pollard, T. D. Aip1 promotes actin filament severing by cofilin and regulates constriction of the cytokinetic contractile ring. *J Biol Chem* **290**, 2289–300 (2015).

[49] Pollard, T. D. Rate constants for the reactions of ATP- and ADP-actin with the ends of actin filaments. *J Cell Biol* **103**, 2747–2754 (1986).

[50] Peskin, C. S., Odell, G. M. & Oster, G. F. Cellular motions and thermal fluctuations: the brownian ratchet. *Biophys J* **65**, 316–324 (1993).

[51] Laird, J. E., Rosenbloom, P. S. & Newell, A. Towards chunking as a general learning mechanism. *AAAI* 188–192 (1984).

[52] Kudryashov, D. S. & Reisler, E. ATP and ADP actin states. *Biopolymers* **99**, 245–256 (2013).

[53] Cao, W., Goodarzi, J. P. & De La Cruz, E. M. Energetics and kinetics of cooperative cofilin-actin filament interactions. *J Mol Biol* **361**, 257–67 (2006).

[54] Chan, C., Beltzner, C. C. & Pollard, T. D. Cofilin dissociates Arp2/3 complex and branches from actin filaments. *Curr Biol* **19**, 537–545 (2013).

[55] De La Cruz, E. M. How cofilin severs an actin filament. *Biophys Rev* **1**, 51–59 (2009).

[56] McCullough, B. R., Blanchoin, L., Martiel, J. L. & De La Cruz, E. M. Cofilin increases the bending flexibility of actin filaments: implications for severing and cell mechanics. *J Mol Biol* **381**, 550–558 (2008).

[57] Suarez, C. *et al.* Cofilin tunes the nucleotide state of actin filaments and severs at bare and decorated segment boundaries. *Current Biology* **21**, 862–8 (2011).

[58] Bibeau, J. P. *et al.* Twist response of actin filaments. *Proc Natl Acad Sci U S A* **120**, e2208536120 (2023).

[59] McCullough, B. R. *et al.* Cofilin-linked changes in actin filament flexibility promote severing. *Biophys J* **101**, 151–159 (2011).

[60] Das, P., Ilyin, V. & Procaccia, I. Instabilities of time-averaged configurations in thermal glasses. *Phys Rev E* **100**, 062103 (2019).

[61] Lavenda, B. H. *Statistical Physics* Dover edn (Dover Publications, Garden City, New York, 1991).

[62] Mullins, R. D., Heuser, J. A. & Pollard, T. D. The interaction of Arp2/3 complex with actin: nucleation, high affinity pointed end capping, and formation of branching networks of filaments. *Proc Natl Acad Sci U S A* **95**, 6181–6186 (1998).

[63] Isambert, H. *et al.* Flexibility of actin filaments derived from thermal fluctuations. effect of bound nucleotide, phalloidin, and muscle regulatory proteins. *J Biol Chem* **270**, 11437–11444 (1995).

[64] Hoyer, M., Crevenna, A. H., Correia, J. R. C., Quezada, A. G. & Lamb, D. C. Zero-mode waveguides visualize the first steps during gelsolin-mediated actin filament formation. *Biophys J* **121**, 327–335 (2022).

[65] Kim, T., Hwang, W. & Kamm, R. D. Computational analysis of a cross-linked actin-like network. *Exp Mech* **49**, 91–104 (2007).

[66] Gittes, F., Mickey, B., Nettleton, J. & Howard, J. Flexural rigidity of microtubules and actin filaments measured from thermal fluctuations in shape. *J Cell Bio* **120**, 923–934 (1993).

[67] Smith, B. A., Daugherty-Clarke, K., Goode, B. L. & Gelles, J. Pathway of actin filament branch formation by Arp2/3 complex revealed by single–molecule imaging. *Proc Natl Acad Sci U S A* **110**, 1285–1290 (2013).

[68] Wear, M. A., Yamashita, A., Kim, K., Maéda, Y. & Cooper, J. A. How capping protein binds the barbed end of the actin filament. *Curr Biol* **13**, 1531–7 (2003).

[69] Hayakawa, K., Sekiguchi, C., Sokabe, M., Ono, S. & Tatsumi, H. Real-time single-molecule kinetic analyses of AIP1-enhanced actin filament severing in the presence of cofilin. *J Mol Biol* **431**, 308–322 (2019).

[70] Khan, S., Conte, I., Carter, T., Bayer, K. U. & Molloy, J. E. Multiple CaMKII binding modes to the actin cytoskeleton revealed by single–molecule imaging. *Biophys J* **111**, 395–408 (2016).

[71] Roland, J., Berro, J., Michelot, A., Blanchoin, L. & Martiel, J. L. Stochastic severing of actin filaments by actin depolymerizing factor cofilin controls the emergence of a steady dynamical regime. *Biophys J* **94**, 2082–2094 (2008).

[72] Wioland, H. *et al.* ADF/cofilin accelerates actin dynamics by severing filaments and promoting their depolymerization at both ends. *Curr Biol* **27**, 1956–1967 (2017).

[73] Medwedeff, E. *Approximate Simulations of Dynamical Graph Grammars using the Dynamical Graph Grammar Modeling Library.* Ph.D. thesis, University of California, Irvine and San Diego State University, San Diego (2024).

[74] Medwedeff, E. & Mjolsness, E. Advances in the simulation and modeling of complex systems using dynamical graph grammars. *arXiv* (2024).

[75] Chu, J.-W. & Voth, G. A. Coarse-grained modeling of the actin filament derived from atomistic-scale simulations. *Biophys J* **90** (2006).

[76] Mjolsness, E. Symbolic neural networks derived from stochastic grammar domain models. Tech. Rep., University of California, San Diego (1997).